applied sciences

MDPI

Article

Enhancement of Energy Harvesting Performance by a Coupled Bluff Splitter Body and PVEH Plate through Vortex Induced Vibration near Resonance

Wei Ken Chin [1], Zhi Chao Ong [1,2,*], Keen Kuan Kong [1], Shin Yee Khoo [1], Yu-Hsi Huang [3] and Wen Tong Chong [1]

1 Department of Mechanical Engineering, Engineering Faculty, University of Malaya, Kuala Lumpur 50603, Malaysia; firelord1117@siswa.um.edu.my (W.K.C.); keenkuan@gmail.com (K.K.K.); khooshinyee@um.edu.my (S.Y.K.); chong_wentong@um.edu.my (W.T.C.)

2 Advanced Shock and Vibration Research Group, Applied Vibration Laboratory, Block R, Faculty of Engineering, University of Malaya, Kuala Lumpur 50603, Malaysia

3 Department of Mechanical Engineering, National Taiwan University of Science and Technology, Taipei 106, Taiwan; yhhuang@mail.ntust.edu.tw

* Correspondence: alexongzc@um.edu.my; Tel.: +603-7967-6815

Received: 21 June 2017; Accepted: 4 September 2017; Published: 7 September 2017

Featured Application: This investigation is to improve the Vortex Induced Vibration effect in Piezoelectric Vibration Energy Harvester System through structural design and vibrational resonance. The outcome could be featured in a small-scale energy harvesting application that is installed at any location with forced flow.

Abstract: Inspired by vortex induced vibration energy harvesting development as a new source of renewable energy, a T-shaped design vibration energy harvester is introduced with the aim of enhancing its performance through vortex induced vibration at near resonance conditions. The T-shaped structural model designed consists of a fixed boundary aluminum bluff splitter body coupled with a cantilever piezoelectric vibration energy harvesters (PVEH) plate model which is a piezoelectric bimorph plate made of a brass plate sandwiched between 2 lead zirconate titanate (PZT) plates. A 3-dimensional Fluid-Structure Interaction simulation analysis is carried out with Reynolds Stress Turbulence Model under wind speed of 7, 10, 12, 14, 16, 18, 19, 20, 22.5, and 25 m/s. The results showed that with 19 m/s wind speed, the model generates 75.758 Hz of vortex frequency near to the structural model's natural frequency of 76.9 Hz. Resonance lock-in therefore occurred, generating a maximum displacement amplitude of 2.09 mm or a 49.76% increment relatively in vibrational amplitude. Under the effect of resonance at the PVEH plate's fundamental natural frequency, it is able to generate the largest normalized power of 13.44 mW/cm^3g^2.

Keywords: vortex induced vibration; vibrational energy harvesting; forced wind; piezoelectric plate system

1. Introduction

In the past, vibration energy harvesting (VEH) had been utilized to power small-scale devices such as sensors and instruments. Many studies have been conducted throughout the years to improve the efficiency and capacity of current vibration harvesting systems, the ultimate goal of which has been to the remove the power source or battery required for small usage. Transducers are used to convert ambient vibration energy sources into electrical energy. The most common transducers are electrostatic, electromagnetic and piezoelectric. Electromagnetic transducers use electromotive force that is created

through change in magnetic flux when vibrational force is induced [1]. Piezoelectric harvesters convert mechanical strain into electrical energy. Efforts had been put into increasing the efficiency and output of a piezoelectric system—some research fine tunes the resonant frequencies while some combines both electromagnetic and piezoelectric systems into a hybrid system which effectively increases the bandwidth of the optimum operating frequencies [2]. In this research relating to flow induced vibration, piezoelectric harvesting is the go-to method of VEH and thus this investigation is aimed at improving performance through the amplification of force while fine tuning the vortex frequency towards the natural frequency of the model.

Flow induced motion (FIM) is a physical phenomenon that occurs when a body is placed in a transverse flow. Vortex induced vibration (VIV) is the most common occurrence of FIM mainly caused by periodic lift forces induced by the flow shedding of bluff bodies [3]. VIV exists through a wide range of velocities whereby the vortex frequency synchronizes with the oscillating frequency of the vibrating object. Extensive studies on VIV and its effects have been carried out throughout the years and the phenomenon is well explained in many comprehensive reviews published in [4–7]. Naudascher and Rockwell identified the 3 types of VIV excitation: movement-induced excitation (MIE), extraneously-induced excitation (EIE) and instability-induced excitation (IIE). MIEVIV arises from the movement of structures exciting the flow in contact. EIEVIV is caused by fluctuating velocities and pressures independent of flow instabilities such as flow turbulence, machine vibrations and earthquake. IIEVIV is caused by flow instabilities due to the presence of bluff body in a transverse flow. VIV was once considered a threat to structural designs such as bridges, buildings, stacks, cables, pipelines and many more [8], but as technology advances in recent years the VIV phenomenon is utilized as a new form of renewable energy source. Wind turbines have been exhaustively researched throughout the years and nowadays VIV energy harvesting is seen as a new form of a smaller and more robust energy harvesting method related to fluid flow.

MIEVIV and IIEVIV energy harvesting concepts were usually the main focus of research with MIE harvesters discussed exhaustively. Vortex induced vibration aquatic clean energy (VIVACE) was the first MIEVIV based harvester developed by Bernitsas et al., which involves a cylinder connected to a generator through the installation of a spring [9]. Raghavan et al., Lee et al., Sun et al. and Zhang et al. show that optimizing fluid flow speed, mass ratio, aspect ratio, damping ratio and surface roughness were contributing to improvement of the VIVACE system [10–14]. Ding et al. proved that a cylindrical and trapezoidal shaped MIEVIV harvester system was the better performing out of all shapes designed [15]. Sayeed et al. studied the flow effects of a step cylinder where different sizes of cylinder produced different vortex frequencies [16]. Karbasian et al. developed an airfoil shaped MIEVIV harvesting system that involves both the heaving and pitching motions of airfoil, improving VIV motion through structure and flow instability [17,18]. Shan et al. studied the bending and torsion vibration effect of a VIV energy harvester [19]. Evolving from a MIE harvester system is the EIE harvester, which involves a dual- or multiple-cylinder system. Side-by-side and tandem arrangement VIV harvesters utilize MIE on upstream bodies while downstream bodies experience EIEVIV [20–23]. It is proven that with optimum gap ratios and position of downstream cylinders the VIV performance significantly improved compared to a single cylinder MIE system. Besides the gap between 2 cylinders, Derakhshandeh et al. showed that the gap ratio between a rigid wall and 2 cylinders also has a dynamic behavior impact towards vortex induced vibration [24].

Although MIEVIV harvesting system is being widely researched and improved, the disadvantage is that the system is slightly complex and installation area focused in rivers or oceans with consistent flow. A less explored IIEVIV energy harvesting system is an alternative VIV harvester system that is less complex without the need for springs and generators, and more robust in locations to be installed. Usually, an IIEVIV energy harvesting system harnesses the vibration from flow instabilities through a piezoelectric plate. Different orientation and designs of IIEVIV energy harvesting systems have been developed throughout the years to enhance the performance of the system. A few significant examples of these are listed below.

Goushcha et al. tested IIEVIV performance of a single thin Mylar and Acrylic cantilever plate with different mounting angles in which a transverse to flow 90° installation yields the highest vibration [25]. McCarthy et al.'s IIEVIV system design is a polypropylene tree leaf design installed with a hinge connecting to the piezoelectric plate aimed at increasing the overall elasticity of the system [26–28]. As only a single elastic plate or system is present in both Goushcha et al. and McCarthy et al.'s IIEVIV energy harvesting models, vortex excitation from flow shedding is only achievable with initial plate deformation or the orientation angle of the plate relative to flow. A large aspect ratio bluff body installed upstream is found to be able to generate flow shedding that excites VIV on the elastic plate. A version of the IIEVIV energy harvesting system had the bluff body installed at the tip of a cantilever plate instead of the base with the purpose of reducing the natural frequency of the model while providing surface width for flow shedding occurrence downstream of the model. Akaydin et al., Dai et al., Huynh et al. and Alhadidi et al. designed and enhanced the IIEVIV harvester [29–32]. Song et al. doubled the system by combining two cylinders with the piezoelectric harvesters, showing improvement in power produced [33]. This version of IIEVIV energy harvester vibration heavily depends on the movement of the tip mass under the effect of VIV. Additionally, installing a heavy body at the tip of the cantilever plate will induce a mass loading effect and cause damage to the elastic plate after some time. In this research, a base bluff splitter body will generate a vortex frequency that affects the vibration of the attached piezoelectric vibration energy harvesters (PVEH) plate. Allen and Smits were the earliest to use a thin cantilever film with attached (Polyvinylidene fluoride) PVDF membrane placed at a distance behind vortex flow for energy harvesting through IIEVIV [34]. However, A PVDF patch is very dependent on the vibration characteristics of the host cantilever plate where only placing at the nodal point with highest strain is able to produce maximum power output. Implementing the advantages of each design above while improving on the disadvantages, the IIEVIV energy harvester designed in this research is a T-shaped coupled bluff splitter body and PVEH plate model. The presence of the bluff splitter body is able to improve the flow shedding effect, generating a larger vortex formation area, while the cantilever PVEH plate acts similarly to a vibrating elastic plate when interacting with the vortex thus generating power output without the need to consider the PVDF patch location.

Mentioned above, the coupled bluff splitter body and PVEH plate energy harvester model requires a piezoelectric plate that is thin and elastic and also has the ability to produce larger voltage output compared to a PVDF plate. A piezoelectric bimorph plate proposed by Huang et al. is composed of a brass plate sandwiched between two lead zirconate titanate (PZT) plates. This material is capable of two-way conversion between mechanical and electrical energy with either series or parallel connections [35]. It is realized that a parallel piezoelectric bimorph coupling will generate twice the higher electromechanical conversion efficiency compared with a series coupling [36]. Large voltage is able to be generated through vibrational displacement of the plate especially during resonant frequency where electrical impedance dropped to a local minimum and voltage output is maximized [37,38].

Currently, the piezoelectric bimorph plate used in this research has a relatively higher natural frequency compared to some of the previous research listed above. In order to generate a steady, continuous and high frequency VIV, a higher consistent fluid flow velocity value is needed. Chong et al. introduced the idea of installing a vertical axis wind turbine on top of an exhaust air cooling tower to harness the constant high-speed exhaust air flow for energy harvesting [39–41]. This concept of utilizing forced flow is also suitable for the IIEVIV energy harvesters in this research, as a high-speed constant fluid flow criteria, needed to ensure continuous energy harvesting, in advance maximizing the total energy generated. A conventional upward draft exhaust air cooling tower flow rate can achieve an air discharge velocity of 10 m/s [42].

Due to the lack of research on the IIEVIV energy harvesting method and the potential development this method possesses as the future source of renewable energy, this research is thus aimed at proposing a solution for IIEVIV energy harvester enhancement for the shortcomings listed above. A fixed T-shaped coupled bluff splitter body and PVEH plate model is introduced because the introduction

of a bluff splitter body is aimed at enhancing the vortex generated from flow shedding. The wide bluff splitter body is able to shed or separate flow, while providing a sufficient area for clear vortex formation around the PVEH plate model. Larger pressure difference is then induced during vortex occurrence and results in a stable vortex frequency acting by the side of the plate. The structural model is then improved by optimizing wind speeds in order to generate maximum VIV, utilizing the resonance effect. The structural model used a thin PVEH plate instead of a PVDF patch to ensure maximum power output generation without the need to determine the location at the host plate that generates the highest strain for maximum voltage production. As the natural frequency of the PVEH plate is relatively higher, the IIEVIV energy harvester is proposed to be more suitably installed at a location with constant high velocity flow—i.e., exhaust air fan or fluid piping—because this encourages consistent VIV generation of the PVEH plate while maximizing the power output. This research is conducted using a FSI simulation to understand the vibrational performance and resulting voltage output of the proposed model when undergoing different high velocity wind speeds, especially when achieving resonance.

In the next section, the theories and calculation methods of vortex induced vibration are mentioned. The third section lists the materials and methodologies applied to conduct the research followed by the results and discussions obtained in the subsequent section. The last section concludes the findings in this research.

2. Theoretical Background

2.1. Criteria for Vortex Induced Vibration Formation

Vortex induced vibration (VIV) occurs only with the fulfillment of the following few criteria. Critical wind speed, v_{crit} is the minimum wind speed for VIV generation and the vortex effect is insignificant when $v_{\text{crit}} < 1.25\, v_{\text{m}}$, where v_{m} is the mean flow velocity [43]. For a certain vibrational mode r, critical wind speed is defined as the wind velocity that creates a vortex shedding frequency equal to the natural frequency of that mode. The formula is given as below:

$$v_{\text{crit},i} = b \times n/\text{St} \tag{1}$$

where b is the fluid-structure contact width, St is the Strouhal number and n is the natural frequency of the model of certain mode r.

Scruton number, Sc, is a dimensionless parameter describing the damping and mass ratio of the structural model. A model with a low Scruton number signifies lower damping and mass ratio value, which encourages VIV occurrence. It was discussed by Tuomo Kärnä that a Scruton number less than 15 is optimum for producing significant VIV [44]. The formula for Scruton Number calculation is shown below [45]:

$$\text{Sc} = 2 \times \delta_s \times m_{r,e}/\rho \times b^2 \tag{2}$$

where δ is the logarithmic decrement structural damping, $m_{r,e}$ is the mass per length ratio of the model and ρ is the fluid density.

Lastly, the aspect ratio represents the ratio between the width and chord length of the model. Vortex quality is heavily dependent on the aspect ratio value as a vortex tends to be more visible with a larger aspect ratio value. Research conducted by both Stokes et al. and Fail et al. showed that a model with an aspect ratio value of 10 to 20 has a clear and strong definition of a vortex, an aspect ratio value of 5 to 0.5 shows moderate vortex shedding, while an aspect ratio with a value ranging from 0.2 to 0.1 shows a faint sign of vortex [46,47].

2.2. Piezoelectric Harvesters Design

Piezoelectric plates usually have 3 independent elements within the piezoelectric coupling tensor terms, d. First, d_{15} relates towards the shear stress, which is not related towards energy harvesting.

On the other hand, d_{31} and d_{33} indicates types of piezoelectric plate material being used. The first subscript 3 describes that voltage is being generated along the z-axis, i.e., electrodes are being attached perpendicularly to the surface. The second subscript describes the direction of the stress being applied, 3 being parallel to the voltage line with 1 being perpendicular to the voltage direction. The piezoelectric plate type 31 is the most common cantilever types PVEH where a bend in PVEH plate creates voltage. The constitutive equations for electromechanical coupling piezoelectric materials are given by:

$$\{S\} = \left[s^E\right]\{T\} + [d]\{E\} \tag{3}$$

$$\{D\} = [d]^t\{T\} + \left[\varepsilon^T\right]\{E\} \tag{4}$$

Or:

$$\{T\} = \left[c^E\right]\{S\} - [e]\{E\} \tag{5}$$

$$\{D\} = [e]^t\{S\} + [\varepsilon^s]\{E\} \tag{6}$$

where $\{T\}$ is stress vector in x, y, z, yz, xz, xy directions, $\{S\}$ is strain vector in x, y, z, yz, xz, xy directions, $\{D\}$ is electric displacement vector in x, y, z directions, $\{E\}$ is electric field vector in x, y, z directions, $[s^E]$ is compliance matrix evaluated at constant electric field, $[d]$ is piezoelectric matrix relating strain/electric field, $[\varepsilon^T]$ = dielectric matrix evaluated at constant stress, $\left[c^E\right] = \left[s^E\right]^{-1}$ is stiffness matrix evaluated at constant electric field, $[e] = \left[s^E\right]^{-1}[d]$ is piezoelectric matrix relating stress/electric field, $\left[\varepsilon^S\right] = \left[\varepsilon^T\right] - [d]^t\left[s^E\right]^{-1}[d]$ is dielectric matrix evaluated at constant strain [48].

2.3. Vibrational Mechanics

Vortex induced vibration of a plate is a form of response from a forced harmonics excitation. In order to simplify the calculation, the plate is assumed to vibrate linearly in single degree of freedom. Considering the structure is an energy harvesting piezoelectric structure, a piezoelectric component should be considered [49]. Therefore, the general forced vibration response for a linear equation can be expressed as followed:

$$[M]\{\ddot{y}(t)\} + [C]\{\dot{y}(t)\} + [K]\{y(t)\} + [\theta]\{V(t)\} = \{F(t)\} \tag{7}$$

where y is the forced response, $[M]$ is the mass matrix, $[C] = \alpha[M] + \beta[K]$ is the proportional damping matrix, $[K]$ is the stiffness matrix, θ is the coupling coefficient and $V(t)$ is electrode voltage and $\{F(t)\}$ is the force excitation vector. According to Tabesh et al., the term $[\theta]\{V(t)\}$ is related to electrical damping and stiffness when the electrodes are connected to a resistive load, R. Equation (8) shows the electromechanical output when a resistive load, R is connected where I is current [50].

$$-V(t) = IR = R\theta\dot{y}(t) + RC_p\dot{V}(t) \tag{8}$$

Equation (7) is re-written as:

$$[M]\{\ddot{y}(t)\} + [C + C_e]\{\dot{y}(t)\} + [K + K_e]\{y(t)\} = \{F(t)\} \tag{9}$$

Noted that the coupling coefficient, θ and the electrical capacitance, C_p for a given dimension of piezoelectric plate, (i.e., L is length, W is width, and T is thickness) are defined as:

$$\theta = \frac{3d_{31}LW}{4\varepsilon_{33}^T T} \tag{10}$$

$$C_p = \frac{\varepsilon_{33}^S LW}{T} \tag{11}$$

The electrical damping, C_e at frequency, ω could be expressed as:

$$C_e = \frac{RC_p\left(\frac{\theta^2}{C_p}\right)}{1+\left(RC_p\omega\right)^2} \tag{12}$$

and electrical stiffness, K_e at frequency, ω could be expressed as:

$$K_e = \frac{\left(RC_p\omega\right)^2\left(\frac{\theta^2}{C_p}\right)}{1+\left(RC_p\omega\right)^2} \tag{13}$$

The flutter and lift force by vortex is undergoing harmonic excitation the force excitation matric, $\{F(t)\}$ can be expressed in terms of excitation frequency, ω and time, t shown in Equation (14):

$$\{F\} = \{P\}\cos(\omega t) \tag{14}$$

A solution in terms of location amplitude vector, $y(t)$ hence can be solved from Equation (9) as:

$$\{y(t)\} = \frac{\{P\}\cos(\omega t)}{(K+K_e-\omega^2 M)+j\omega(C+C_e)} \tag{15}$$

The average power produced from a PVEH plate can be expressed as:

$$P_{avg} = \frac{R\omega^2\theta^2{y_t}^2}{2\left(1+(RC\omega)^2\right)} \tag{16}$$

When considering y_0 as a function of load, R based on Equation (15) above and the average power equation, as shown in Equation (16), the optimum power with respect to R is obtained as:

$$R_{opt} = 2\zeta/C_p\omega\sqrt{4\zeta^2+\theta^4} \tag{17}$$

Such a system is too complicated to be useful for an analytical design. In addition, the coupling effect of θ is assumed to be relatively small and weak and Equation (17) can be simplified as:

$$R_{opt} = 1/C_p\omega. \tag{18}$$

2.4. Optimizing Power Performance

A piezoelectric harvester receives input in the form of amplitude and frequency from a vibrational source. Tabesh et al. described a 2-step method used to optimize the power performance of a PVEH plate as follows:

- Maximizing the extracted electric power for a fixed deflection by matching the resistive load. It is a sub-optimal condition for a matched resistive load, assuming that y_0 is not a function of R.
- Maximizing the deflection for the matched resistor as derived in Equation (16).

At this stage, maximum deflection is achieved under matched natural frequency with excitation frequency as well as considering the optimal resistance. [50]. It is also mentioned that optimizing the electric power assuming a fixed deflection at the resonance frequency of the system does not severely impact the accuracy of the calculation compared with the exact numerical solution of the model.

To obtain the optimum harvested electric power through largest deflection, it is important to ensure maximum deflection under the matched vibration frequency, ω, with natural frequency as well as using the optimal resistance, $R_{opt} = 1/C_p\omega$ [33]. The optimum resistance value is applied to

Equations (12) and (13) to obtain the electrical damping and stiffness, thus yielding the maximum deflection, y_{max}, from Equation (15) as shown below:

$$y_{max} = \frac{P}{\left(K + \frac{\theta^2}{2C_p} - \omega^2 M\right) + j\omega\left(C + \frac{\theta^2}{2C_p\omega}\right)} \tag{19}$$

Applying optimal resistance, R_{opt} to the average power equation in Equation (16), optimum power, P_{opt} is generated from the maximum voltage, V_{max} harvested under the maximum tip deflection, y_{max}. The optimum power, P_{opt} can be expressed as:

$$P_{opt} = \frac{\omega\Theta^2 {y_{max}}^2}{4C_p} \tag{20}$$

Or:

$$P_{opt} = \frac{{V_{max}}^2}{R} \tag{21}$$

3. Materials and Methods PVEH Model

3.1. PVEH Model

The PVEH is made of piezoceramic material (i.e., lead zirconate tirtanate or PZT), which has dimensions of 57 mm in length, 0.51 mm in thickness, and 31.8 mm in width. The details of the properties and performance regarding this PVEH (model: T220-A4-503X) are given by the manufacturer Piezo System Inc., Woburn, MA, USA. The name of the PVEH is PSI-5A4E corresponding to PZT-5A. The PVEH is a piezoelectric bimorph plate which consists of 3 layers, where the top and bottom layers are made of PSI-5A4E while the middle layer is a brass shim layer served as a reinforcement layer shown in Figure 1. PSI-5A4E is an industry type 5A (Navy Type II) piezoceramic. Thin vacuum sputtered nickel electrodes produce extremely low current leakage and low magnetic permeability. The thickness of each layer and construction of the PVEH plate is shown in Figure 2. The layers are held together with glue but the thickness of the glue is ignored. The capacitance value provided for this configuration of PVEH plate is 73 nF.

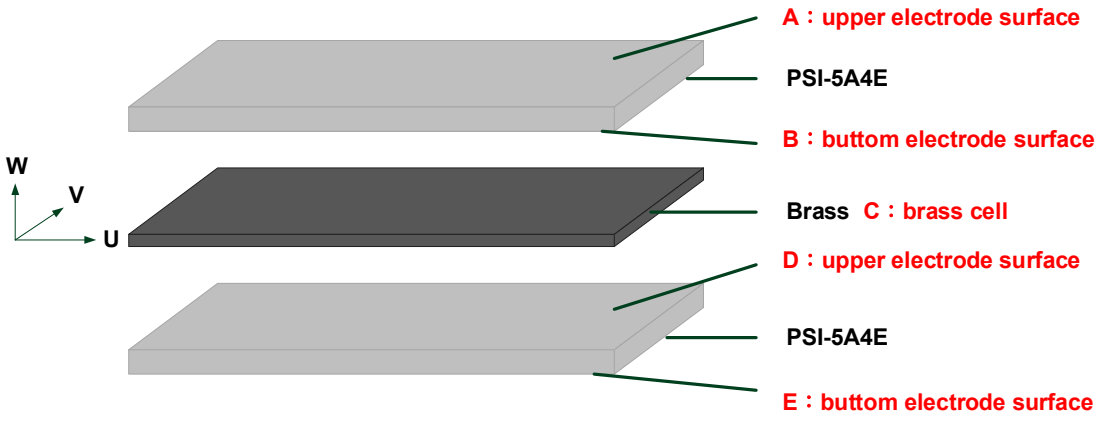

Figure 1. Construction and material properties of the piezoelectric vibration-based energy harvester (PVEH) plate.

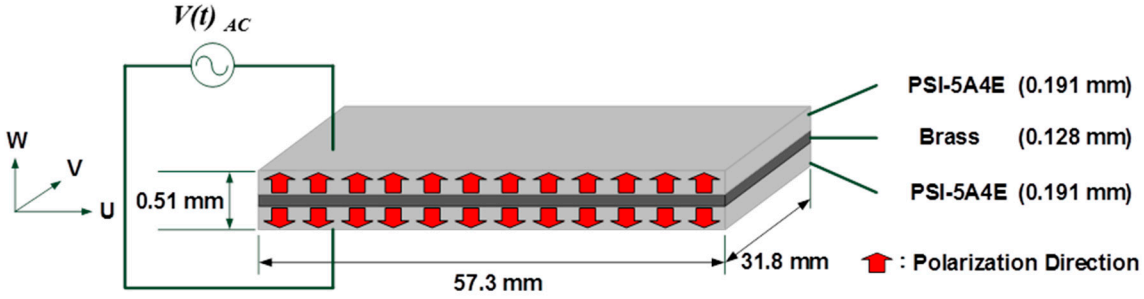

Figure 2. Thickness and construction of the PVEH plate.

3.2. Design and Modelling

The fluid-structure interaction (FSI) simulation technique was used to investigate the vibrational performance of the coupled bluff splitter body and PVEH plate under different wind speeds. The FSI simulation requires the setup of both Computational Fluid Dynamics (CFD) and Computational Structural Dynamics (CSD) separately before data coupling setup. The T-shaped structural model is divided into two separate parts: thin elastic PVEH plate and bluff splitter body. As mentioned in Section 1, the PVEH plate with bimorph properties is constructed from a brass plate sandwiched between two PZT plates with a total dimension of 31.8 × 57 × 0.51 mm. The PVEH plate is placed onto the fixed boundary condition aluminum bluff splitter body with a cantilever boundary condition as shown in Figure 3. The detailed dimension and material properties of both PVEH plate and bluff splitter body are displayed in Table 1. The large base plate was designed so that a clear vortex is formed and presented at the side of the PVEH plate results in a stable vortex frequency for the purpose of VIV effect enhancement. Meanwhile, the longest and largest surface area of PVEH plate was chosen for its lower elastic properties and larger area of contact with vortex.

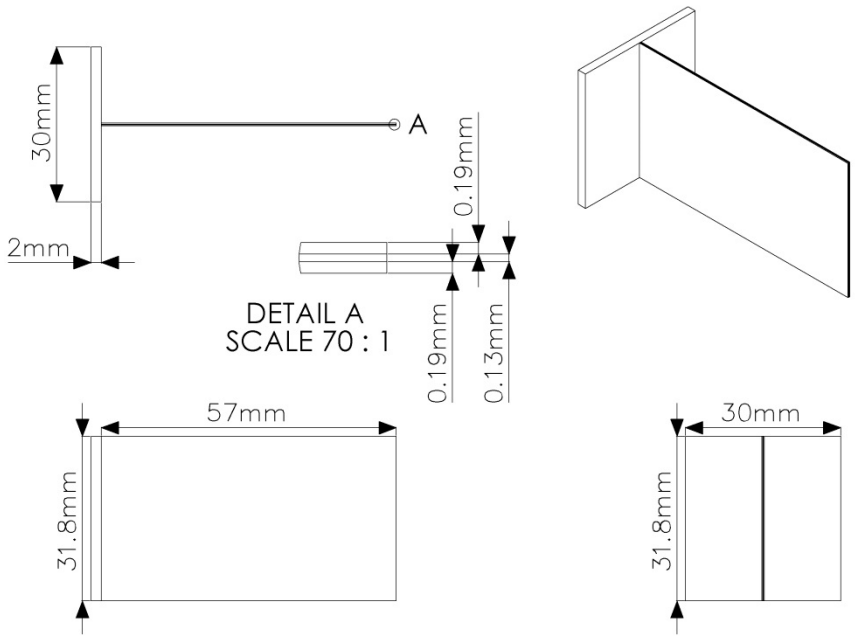

Figure 3. Structural model design of coupled bluff splitter body and elastic PVEH plate.

Table 1. Material properties of structural model.

Material Properties	Piezoelectric Plate (Brass)	Piezoelectric Plate (PZT)	Aluminum Bluff Splitter Body
Model Dimensions	31.8 × 57 × 0.13 mm thick	31.8 × 57 × 0.19 mm thick	31.8 × 30 × 2 mm thick
Density	8830 kg/m^3	7800 kg/m^3	2770 kg/m^3
Young's Modulus	1.03×10^{11} Pa	x-direction—6.6×10^{10} Pa y-direction—6.6×10^{10} Pa z-direction—5.2×10^{10} Pa	7.1×10^{10} Pa
Poisson's Ratio	0.34	x-direction—0.31 y-direction—0.242 z-direction—0.242	0.33
Piezoelectric Constants	-	$d_{15} = 550$ pm/V $d_{31} = -190$ pm/V $d_{33} = 390$ pm/V	-
Dielectric Constants	-	$\varepsilon^S_{11} = 11.12$ nF/m $\varepsilon^S_{33} = 14.02$ nF/m	-

Besides the structural model, an appropriate sized fluid domain was also designed for CFD analysis during the modelling phase. Distance from surrounding domain wall or inlet to the edge of the structural model should be equal to or more than 5D of the structural model where D is the largest width of the model equivalent to 30 mm. The outlet boundary should be set at a distance equal to or more than 10D from the downstream tip of the structural model. As a result, the CFD fluid domain designed had dimensions of 600 mm in length, 400 mm in width and 400 mm thick. The model is placed at the center between top, bottom and side domain walls while located 300 mm from the inlet boundary as illustrated in Figures 4 and 5. The fluid domain also has a 1.4% blockage ratio, which is lower than the standard maximum of 3% when the structural model is placed inside.

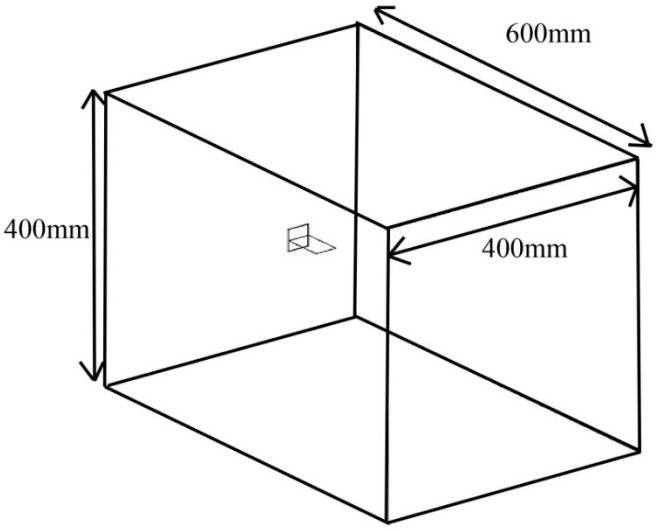

Figure 4. Fluid domain dimension and structural model dimension.

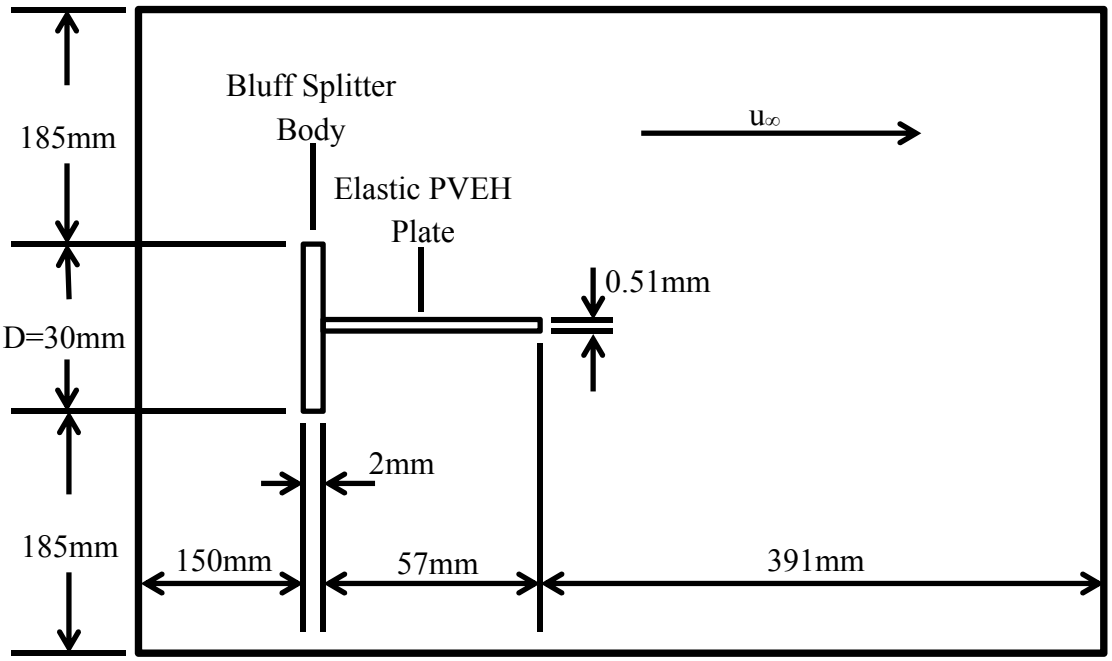

Figure 5. Simulation setup wind direction towards model (D = 30 mm).

3.3. Structural Model Dynamic Characteristics

The Scruton number and aspect ratio of the structural model was adjusted to an optimum value in order to ensure good quality VIV is generated. The PVEH model was designed to have a structural damping ratio of 0.02 and mass per length ratio of 0.14 kg/m. From Equation (2), these values yielded a Scruton number of 24.8 whereby it is slightly higher than the upper boundary limit. Like so, the damping of the piezoelectric model will slightly suppress the vibrational motion caused by vortex.

The T-shaped model designed was to take into account the aspect ratio mentioned by R.J. Fail et al. [46]. With the addition of a bluff splitter body, aspect ratio value of the T-shaped structural model increased from 0.00912 to 15 compared to only a single PVEH plate as shown in Figure 3. Hence, the inclusion of a bluff splitter body coupled with the PVEH plate will increase the quality of vortex produced because flow separation area is larger, providing a larger low pressure region generating vortex and thus a larger lift force will be acting on the surface of the PVEH plate.

3.4. Mesh Generation

The grid for this research was generated using the built-in ICEM meshing module in the commercial ANSYS software, ANSYS Inc., Canonsburg, PA, USA. For the entire structural model, the mesh size applied is a 0.001 × 0.001 m structured quadrilateral mesh. The mesh generated for the structural part shown in Figure 6d owns a total of 50,709 nodes and 7392 elements with mesh skewness near zero. On the other hand, a CFD domain mesh was applied with 0.001 to 0.2 m of unstructured tetrahedral mesh depending on the closeness to the structural model's FSI interface as shown in Figure 6a. The FSI interface wall boundary surrounding the model in CFD had an equal grid size of 0.001 m integrated with 10 layers of inflation layer displayed in Figure 6b,c respectively. A total of 98,148 nodes and 325,010 elements were generated with maximum skewness reaching 0.78.

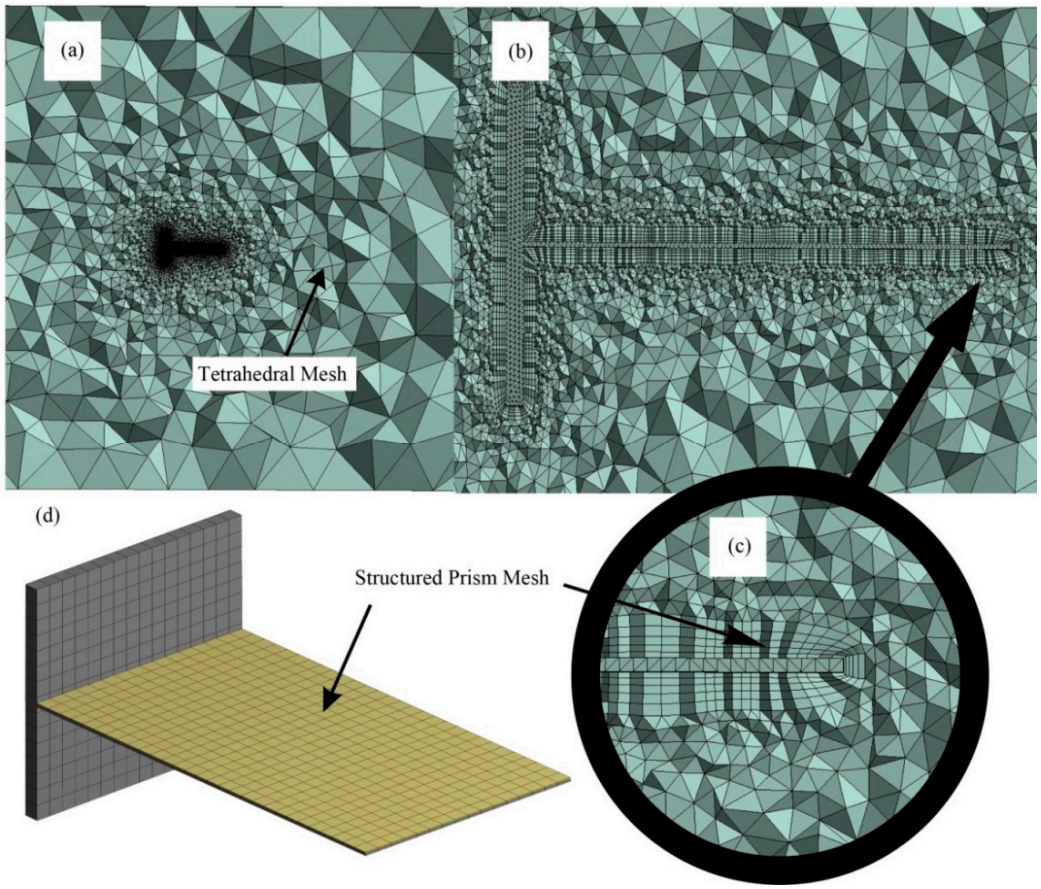

Figure 6. (**a**) Unstructured fluid domain mesh; (**b**) inflation layer near wall of model; (**c**) close-up on tip of model with inflation layer; (**d**) structured mesh on model.

3.5. CFD Boundary Condition

Figure 5 above also represents the schematic setup of the CFD simulation for 6 different subsonic inlet velocity test cases of 7, 10, 12, 14, 16, 18, 19, 20, 22.5 and 25 m/s set at the inlet boundary. Outlet pressure was set as 101,365 Pa at the outlet boundary similar to atmospheric pressure. Air with density, $\rho_f = 1.82 \times 10^{-4}$ kg/m^3 and viscosity, $\mu_f = 1.18 \times 10^{-3}$ was set as the medium passing through the domain with constant temperature of 298.15 K. The wall boundary surrounding the structural model was applied with fluid-structure interface boundary to allow data exchange between CFD and CSD solver. The top, bottom and side domain walls were set as non-slip wall boundaries respectively. The overall fluid domain was a stationary domain, however, mesh movements were allowed when interacting with the displacement of structural model.

3.6. Numerical Procedure

The CFX and Mechanical APDL module with Piezoelectric Extension added under commercial ANSYS software were used to conduct this research. The turbulence model applied in this simulation was the SSG Reynolds-Stress Turbulence model with scalable wall function set because this turbulence model solving transport equations for each Reynolds Stress had proved to work better on flow involving separation and vortex compared to traditional two-equation k-ε and k-ω turbulence model [51]. The ANSYS MultiField option of external solver coupling was chosen to carry out FSI analysis. Transient scheme and advection scheme was both set with Second Order Backward Euler and High Resolution respectively. The FSI coupling for this simulation was a strong two-way

coupling approach where the exchange of data between structural and CFD module occurred in a single coupling iteration and a converged solution was obtained before moving to the next time step.

The time step size for the run was set at 5×10^{-4} s to run for 0.3 s or equivalent to 600-time steps with 5–10 coupling iterations for each time step. Convergence was achieved when residual reaches the target of 1×10^{-4} with an under-relaxation factor of 0.75. This time step set was able to collect data with a frequency up to 2000 Hz and thus being able to capture frequency range lower than 100 Hz with decent resolution in this simulation conducted. A maximum of 10 iterations in coupling solver and 5 iterations in CFD solver were set for each time step.

The simulation of electrical performance is conducted using the ANSYS Harmonic response module with a Piezoelectric extension. Previous FSI simulation results act as input for obtaining the electrical result considering the vibration of PVEH plate and optimum load resistance. The range of frequency settings were from 20–100 Hz with an interval of 0.2 Hz. The optimum load resistance for simulation study was calculated using Equation (18). The voltage generated for each VIV case was obtained.

3.7. Experimental Setup

An experiment (Figure 7) was set up to obtain the harmonic response of the PVEH plate under certain vibrational frequencies in Section 4.1. A function generator (Figure 7a) was used together with a laser doppler vibrometer (LDV) (Figure 7b) to measure the vibrational displacement. The LDV model used is the PDV-100 by the manufacturer Polytec GmbH Waldbronn. In addition, the electronic speckle pattern interferometry (ESPI) technique was used to measure the transverse and planar vibrations and observe the mode shape of corresponding frequency (Figure 8). ESPI measurement techniques provide a real-time, non-contact and high precision measurement. The detailed ESPI technique experimental setup and performance comparison over other measurement techniques including laser doppler vibrometer (LDV) and impedance analyzer are mentioned Ma and Huang et al. [36,52]. Planar vibration is not considered in this study due to the nature of VIV excitation.

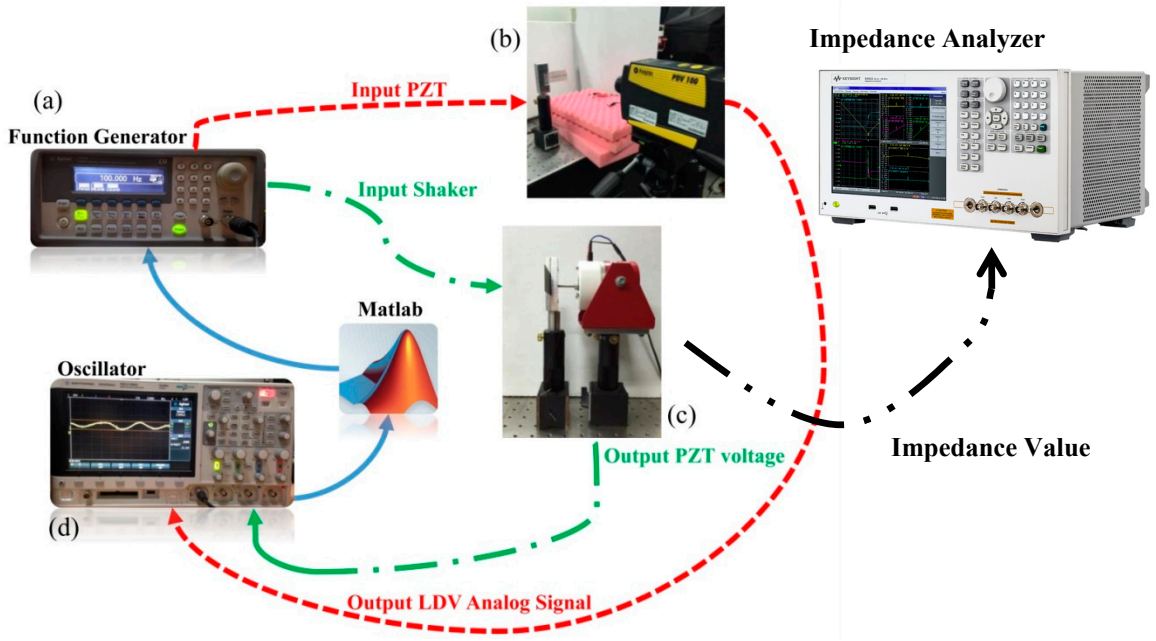

Figure 7. Schematic setup of output voltage under different vibrating frequency.

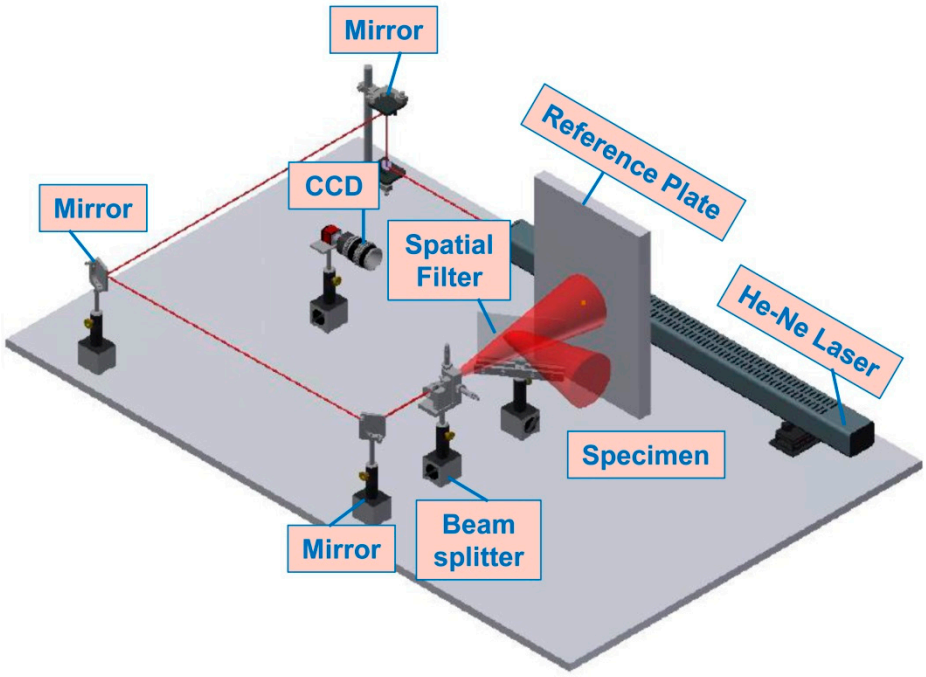

Figure 8. Schematic diagram of electron speckle pattern interferometry (ESPI).

A similar experimental set-up was used to investigate the output voltage of the PVEH plate under certain vibrating frequency and the results are presented in Section 4.6. Shown in Figure 7, an input voltage of 0.5 V was applied by a generator (Figure 7a) to the shaker (Figure 7c) to excite the PVEH plate with frequency range of 0 to 100 Hz. The shaker was connected to the base fixture that clamps the PVEH plate through a rod. The shaker used has a frequency range of 14,000 Hz and is supplied by the Data Physics Corporation, San Jose, CA, USA with the model number V4. An Impedance Analyzer of model E4990A by KeySight Technologies, Wokingham, UK was used to determine the varying load applied onto the circuit to find out the optimum load resistance that produces the highest resulting voltage by that particular vibrational frequency of the PVEH. The resulting voltage under the optimum load was recorded with an oscillator (Figure 7d) and then processed using Matlab, The MathWorks Inc., Natick, MA, USA. The voltage obtained was then used to calculate the normalized optimum power generated by the PVEH at a frequency coupled with optimum resistance applied onto the circuit.

4. Results and Discussions

4.1. Structural Validation

In order to validate the structural model, a modal analysis simulation was done on the PVEH plate model to correlate with the displacement spectrum obtained from experiments ranging from 0 to 4000 Hz using electronic speckle pattern interferometry (ESPI). The simulated modal analysis results from FEM (Figure 9) agreed well with the experimental results obtained in Figure 10 below. The percentage difference shown in Table 2 is small between both simulated and experimental modal analysis results with values ranging from 0.042% to 4.614%. Therefore, the structural model reproduced by the computer aided modelling (CAM) is comparable to the real structure. As the desired frequency range in this research study is low (<100 Hz), only the first two modes were considered for comparisons especially the first mode or first bending mode. This model is thus verified in terms of structural perspective.

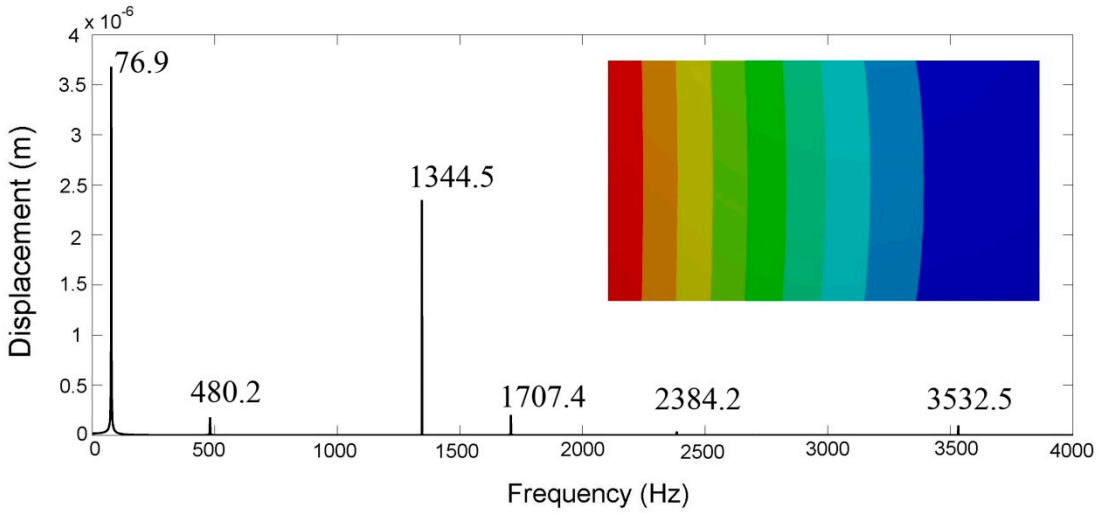

Figure 9. Simulated harmonic response with model of first bending mode at 76.9 Hz.

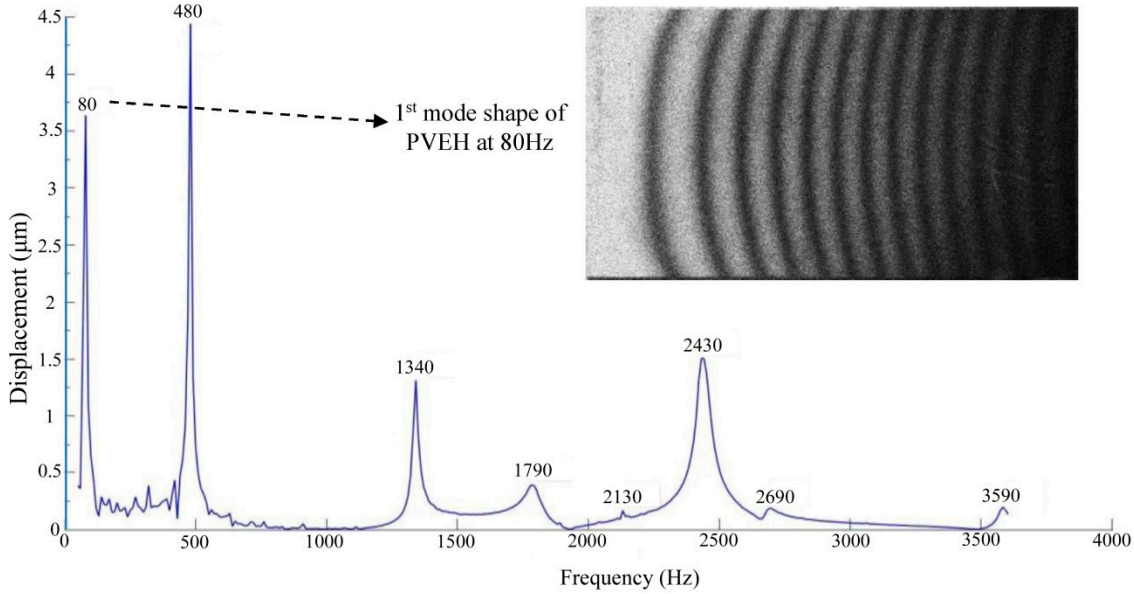

Figure 10. Dynamic characteristic of piezoelectric plate using ESPI and first bending mode contour observed at 80 Hz.

Table 2. Difference between simulated and experimental frequency.

FEM Harmonic Response (Hz)	ESPI (Hz)	Difference (%)
76.9	80	−3.75
480.2	480	0.042
1344.5	1340	0.33
1707.4	1790	−4.614
2384.2	2430	−1.884
3532.5	3590	−1.602

The Modal Analysis simulation results shown in Figure 9 determined that the fundamental frequency of the coupled bluff splitter body and PVEH plate model is a first bending mode at 76.9 Hz having a 3.75% difference to 80 Hz obtained experimentally. The fixed boundary condition bluff splitter body was assumed to be non-contributing to the natural frequencies, thus

not affecting the displacement shape and natural frequencies. Natural frequencies only change with respect to the change of geometrical properties, material properties and boundary conditions. The discrepancy between the experimental and simulated natural frequencies happens when the three parameters mentioned above used in the simulation environment differ from the real structural model. The material properties of the PVEH in real-life may have slight difference as compared with the published material properties used in simulation. Besides, the simulation of clamping mechanism of the PVEH plate may have slight difference as compared with the real clamping device. Although these discrepancies occurred, the result with a percentage difference of lower than 5% is still considered acceptable.

Figure 11 shows the difference in modal analysis results when considering, and without considering, the piezoelectric properties in PVEH plate. When the piezoelectric properties are being considered, the natural frequency shows a higher value, due to the piezoelectric coupling cause the plate to have stiffer properties. This modal analysis result is then act as a base reference during CSD studies in FSI simulation.

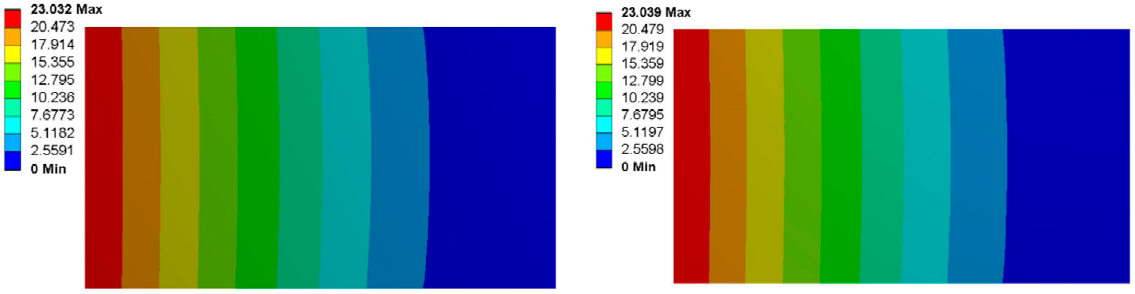

(**a**) (**b**)

Figure 11. Natural frequency from simulation (unit: m); (**a**) without piezo properties = 75.4 Hz; (**b**) with piezo properties = 76.9 Hz.

4.2. Grid Independence Study

Before any simulation research was being done, a grid independence study was carried out in order to verify the outcome obtained is not being affected by the grid size applied. In this research, the grid independence study was conducted in 4 different minimum grid sizes ranging from 0.006 m (20,990 elements), 0.004 m (39,168 elements), 0.002 m (104,721 elements), 0.001 m (325,010 elements) and 0.0005 m (375,598 elements) shown in Figure 12. The grid independence study was conducted using a transient computational fluid dynamics method with 7 m/s inlet flow velocity while domain and turbulence model settings remained the same. By comparing the root mean square value (RMS) of fluctuating lift force acting on the PVEH plate under the effect of VIV, Figure 12 showed that the force value increases from 0.000176 N with 0.006 m mesh size until it reaches 0.00162 N with 0.002 m of mesh size. The results obtained from then onwards had a constant value of around 0.0016 N and 0.0017 N, which is in an acceptable range. From this, the mesh size of 0.001 m in between 0.002 and 0.0005 m was chosen for the reason of higher computational accuracy but less computational cost induced when conducting simulation.

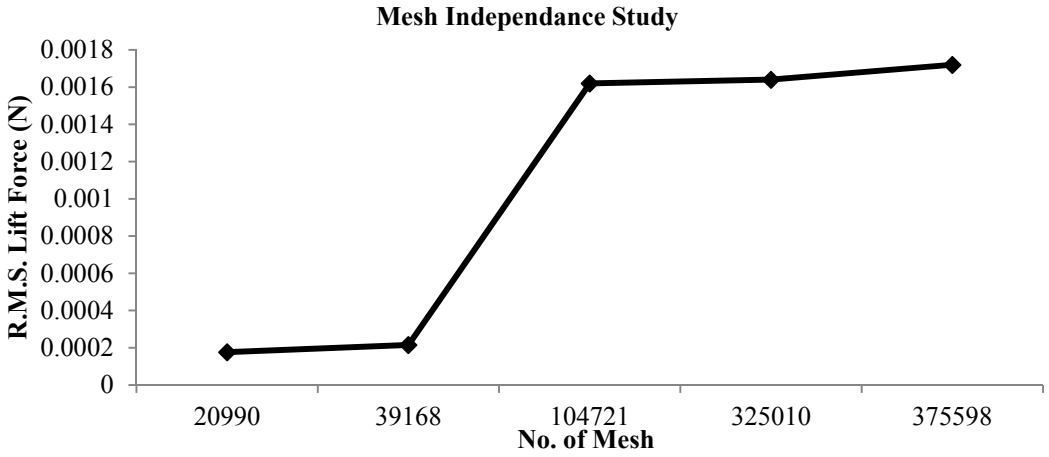

Figure 12. Graph of the mesh independence study.

4.3. Vortex Formation with Bluff Splitter Body

Results shown in Figure 13a–j include the velocity contour of 7, 10, 12, 14, 16, 18, 19, 20, 22.5 and 25 m/s wind speed at time 0.3 s. It is shown in all figures that with constant wind flow, either with a high or a low wind velocity, the model was able to generate a large area of vortex downstream with the introduction of a bluff splitter body. As shown in the contour plot Figure 13, when wind flow was obstructed by upstream bluff splitter body, it separates around the body leaving a low velocity high pressure vortex region illustrated as the blue region downstream of the bluff splitter body in the figure. It is observed that vortex formation length generated under different wind speeds is similar. This proves that similar bluff splitter body shape and structural model's aspect ratio value produces a similar vortex formation length, disregarding the flow speed.

Whenever wind flow passes through a bluff splitter body, the vortex generated will usually cause wake propagation downstream in which the frequency and pressure force will excite and damaged downstream structures. It is mentioned by F.J. Huera-Huarte that a rigid plate installed downstream of a bluff body is able to suppress wake propagation [53]. It is noted in Figure 13 below that by switching the rigid plate to a more flexible PVEH plate provides an additional vibrational tendency under the influence of vortex and in a degree generating power while suppressing further propagation of vortex downstream into wake.

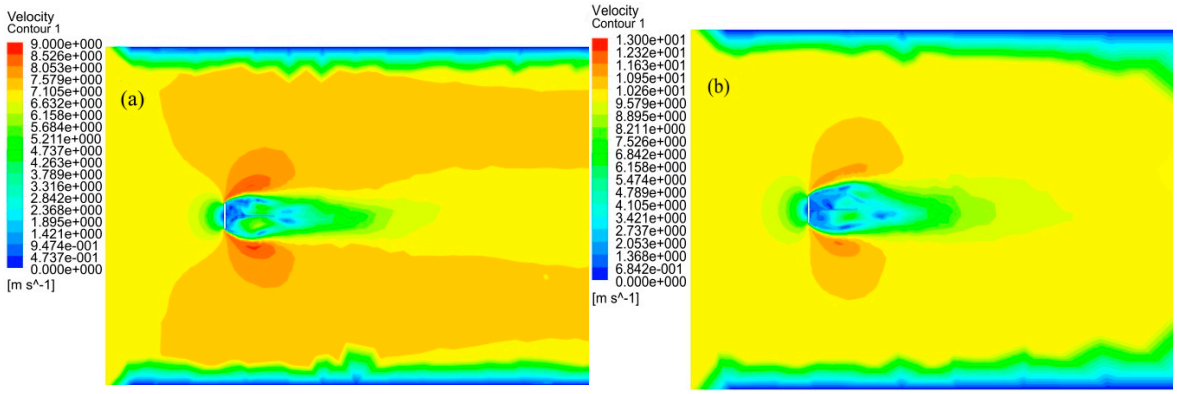

Figure 13. *Cont.*

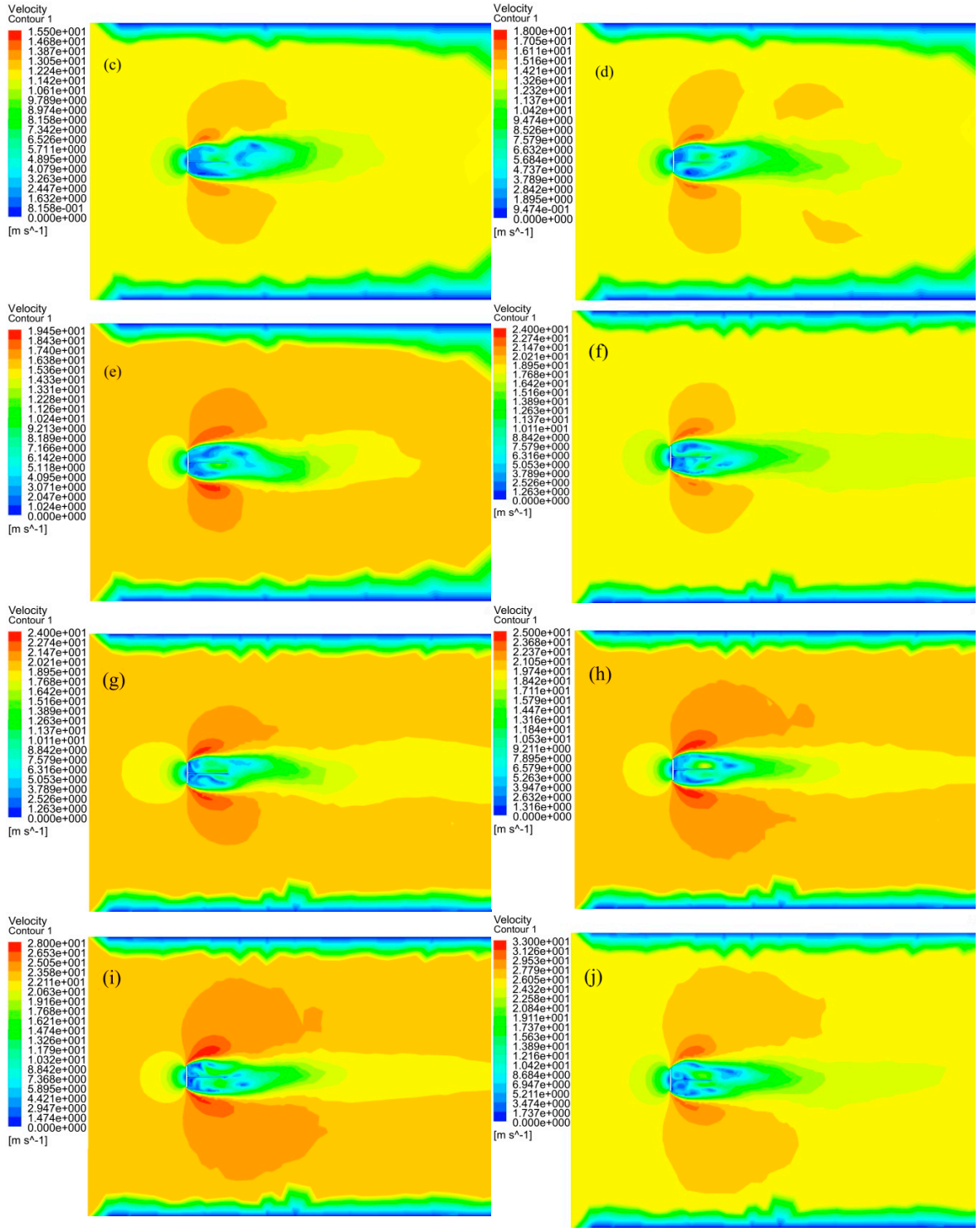

Figure 13. Velocity Contour at 0.3 s with velocity (**a**) 7 m/s; (**b**) 10 m/s; (**c**) 12 m/s; (**d**) 14 m/s; (**e**) 16 m/s; (**f**) 18 m/s; (**g**) 19 m/s; (**h**) 20 m/s; (**i**) 22.5 m/s; (**j**) 25 m/s.

In order to further describe the importance of the bluff splitter body for generating a better quality vortex, Figure 14 below depicts a PVEH plate in magnified view placed in 7 m/s wind speed domain similar to all the settings as previous cases. Without the bluff splitter body, it is shown that unlike in Figure 13, there are no low velocity regions present surrounding the PVEH plate which represents vortex formation. The reason is that bluff splitter body provides enough width which effectively

separates the flow when comes into contact. Besides, wide bluff splitter body provides sufficient area downstream for clear vortex formation around the PVEH plate as shown in the light blue area in Figure 13a–j. Without vortex formation in Figure 14, neither vortex frequency nor fluctuating force is induced thus the PVEH plate is not vibrating under the effect of flow for the period of 600-time steps conducted. In addition, the lift force in this situation is at a constant 1.2×10^{-4} which is comparably lower to the values of models with the bluff body intact and also it is not fluctuating creating frequency value.

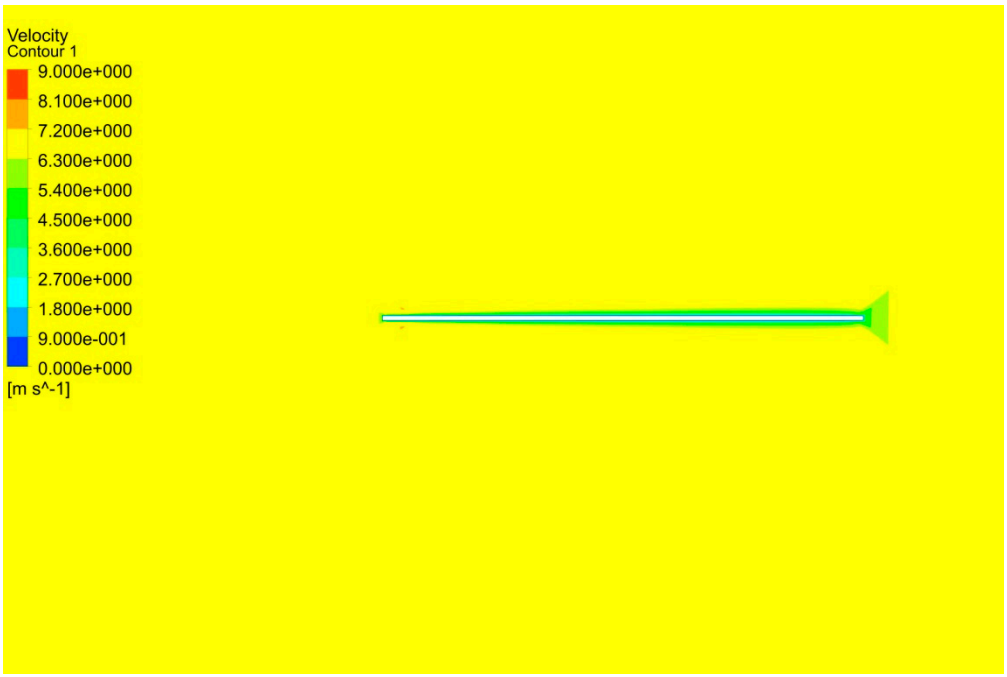

Figure 14. Velocity contour of PVEH plate without bluff splitter body under 7 m/s wind speed.

4.4. Fluctuating Lift Force

Fluctuating lift force refers to the alternating pressure force created by vortex flow acting on the flexible PVEH plate. Figure 15 indicates that with the increase of wind velocity, the fluctuating lift force acting on the PVEH plate is higher. Referring to Bernoulli's principle, this is due to a higher velocity flow generating a lower pressure region of vortex area. Similar to an airfoil wing, a vortex area with lower pressure region generates more lift force acting on the opposite side of the PVEH plate. Vortex occurrence usually is unstable in nature, thus with the installment of a bluff splitter body, fluctuating lift force generated is amplified and more periodic containing a certain vortex frequency after reaching steady condition. Equation (2) denotes that larger wind speeds have a higher vortex frequency generated as a result of the rapid alternating lift force acting on the PVEH plate. The vortex frequency heavily influenced the vibrational frequency and amplitude of the PVEH plate which will be explained in Section 4.5 later.

The graph of the lift force induced under 19 m/s (Figure 16) demonstrates that the amplitude of lift force acting on the PVEH is slightly fluctuating. The phenomenon was determined to be caused by two reasons: first is the simulation research is done with a three-dimensional domain instead of a usual 2D or 3D symmetrical domain which is widely used in most of the simulation research. The three-dimensionality of the flow causes fluctuations in lift force applied on the PVEH model, as tip flow vortex generated at front and back edge of the model exerts different directional force and frequency that disrupted the main vortex flow. Tip speed flow cannot be observed via 2D or symmetrical 3D simulations therefore occasionally being ignored by researchers. Although the contribution of the tip speed vortex is small, it still had a substantial effect on the flow amplitude and

steadiness. The second reason is that the wind flow velocity is located at a high turbulence region of Reynolds number (Re) between 2.33×10^5 and 3.24×10^5. A high turbulence flow consists of high fluctuations in value and uncertainties causing much noise produced around the body.

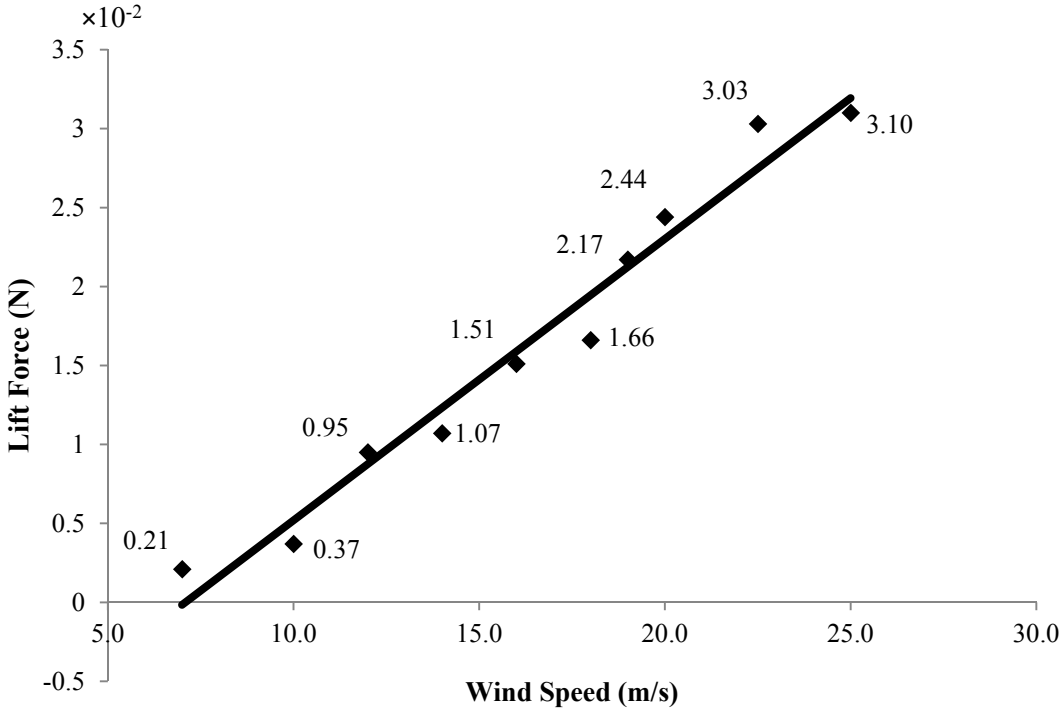

Figure 15. Graph lift force vs. wind speed.

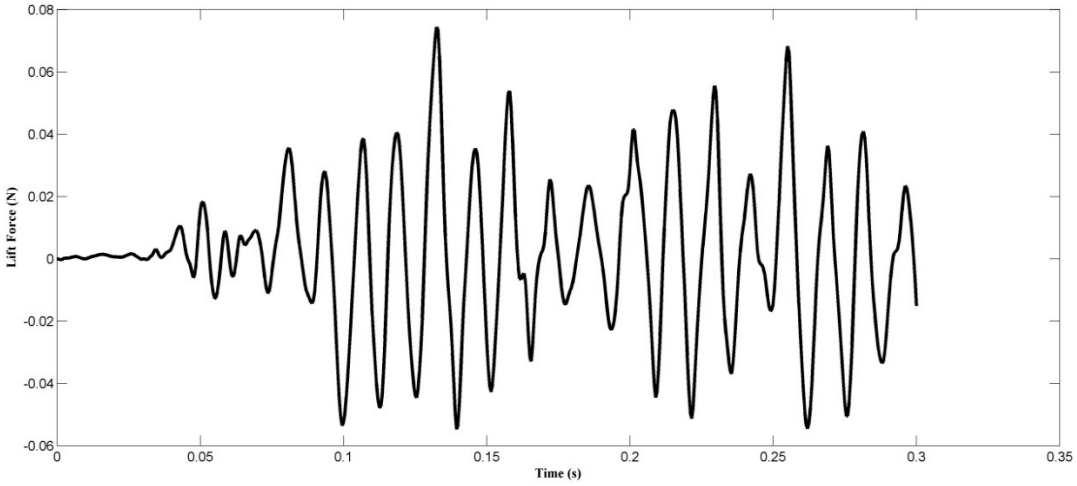

Figure 16. Graph lift force vs time at 19 m/s.

4.5. Vortex Induced Vibration Response

The Strouhal number of the model shown in Table 3 indicated that under high wind speeds, the Strouhal number deviates from the theoretical value calculated by Equation (1). Kovasznay (1949) had mentioned in a proceeding that the theoretical Strouhal number of a model is relevant with a Reynolds number below 10^4 [54]. Therefore, by applying Equation (1), the Strouhal number for a lower Reynolds number of 8.76×10^4 is 0.89, but as the Reynolds number moves to a value more than

1.81×10^5, the Strouhal number increases to a range between 0.108 and 0.12. This value is important in predicting the critical velocity generated from a certain frequency using Equation (1).

Table 3. Wind speed, Reynolds number and Strouhal number.

Wind Speed (m/s)	Reynolds Number	Strouhal Number
7.00	8.76×10^4	0.08580
10.00	1.29×10^4	0.090909
12.00	1.55×10^4	0.104895
14.00	1.81×10^4	0.108225
16.00	2.07×10^4	0.113636
18.00	2.33×10^5	0.117845
19.00	2.46×10^5	0.119618
20.00	2.61×10^5	0.120071
22.50	2.87×10^5	0.111376
25.00	3.24×10^5	0.118297

Mentioned in Section 4.5, it is proven in Table 4 that wind speed magnitude contributes proportionally to the vortex and vibrating frequency of the model, as the higher the wind speed velocity, the higher is the vortex frequency induced. This research observed that vibrational frequency of the PVEH plate always locked-in a similar frequency value to the vortex frequency produced from flow separation across the bluff splitter body. This is because a structure will always be affected and synchronized with the surrounding vibrating frequency it came across. The vortex frequency value thus being similar to the vibrational frequency of PVEH plate induced a high impact on the resultant vortex induced vibration amplitude of the PVEH plate.

Table 4. Difference between vibrational and natural frequency.

Wind Speed (m/s)	Resultant Frequency (Hz)	Natural Frequency (Hz)	Difference (%)
7.00	20.020	76.9	−73.73%
10.00	30.303		−60.59%
12.00	41.958		−45.44%
14.00	50.505		−34.32%
16.00	60.606		−21.19%
18.00	70.707		−8.05%
19.00	75.758		−1.48%
20.00	80.808		+4.04%
22.50	82.418		+7.18%
25.00	100.00		+30.05%

Complete results of tip mesh displacement against time are displayed in Figure 16. In all of the test cases illustrated in Figure 6, the displacement starts from a low and unsteady vibration and reaches a period where the tip displacement value is relatively constant around a range. This is because when vortex is unstable; the starting force due to flow instabilities acting on the PVEH plate is weak and uneven, creating unsteady and smaller tip displacement. From Figure 17a–e, (i.e., 7 to 16 m/s), the tip displacement graph shows non-periodic occurrence after reaching steady condition. This is mostly because the vortex frequency is not near to the natural frequency of the model and the tip displacement is mainly contributed by the fluctuating lift force acting on the PVEH plate. In Figure 17f–h (i.e., 18, 19 and 20 m/s), steady and periodic tip displacement is achieved. This is due to resonance or near resonance phenomena where the vortex frequencies generated by these 3 wind speeds are near to the natural frequency of the model. During resonance, the matched vortex frequency and natural frequency amplifies the tip displacement giving periodic pattern which is purely governed by the damping of the system. Lastly, Figure 17i,j shows a different vibrational curve compared

to other figures, where the pattern is similar to when 2 different frequencies sinusoidal waves are superimposed together. This is because when the model is vibrating between 1st and 2nd natural frequencies, the vibration is contributed by both mode shapes.

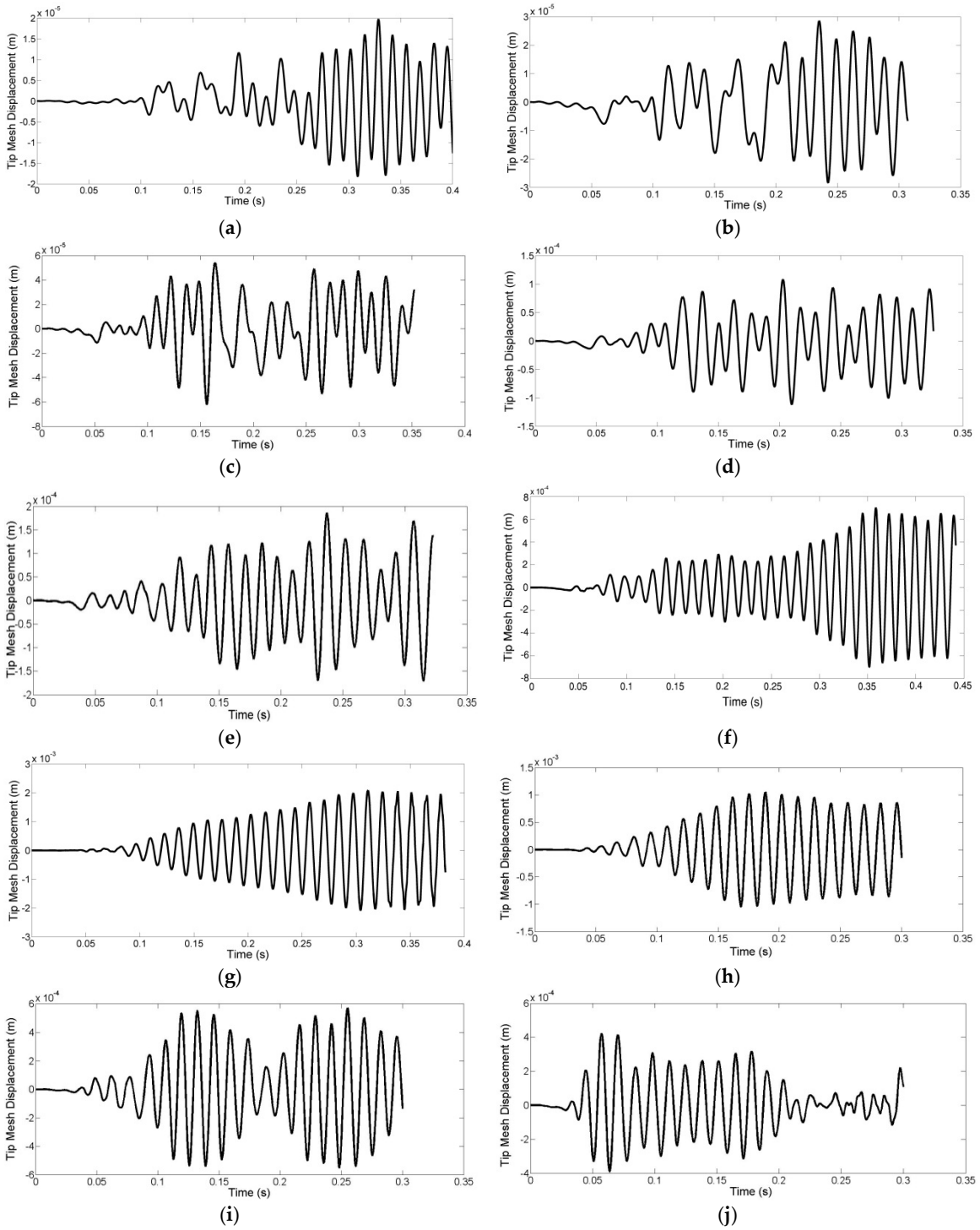

Figure 17. Graph tip mesh displacement (m) against time (s); (**a**) 7 m/s; (**b**) 10 m/s; (**c**) 12 m/s; (**d**) 14 m/s; (**e**) 16 m/s; (**f**) 18 m/s; (**g**) 19 m/s; (**h**) 20 m/s; (**i**) 22.5 m/s; (**j**) 25 m/s.

Structural resonance is a phenomenon defined as maximum structural vibration amplitude when the vibrational frequency of the structure lies near or similar to the model's natural frequency. This is because, in terms of pure structural dynamics, the local amplitude vector can be expressed as:

$$\{y(t)\} = \sum \{\Phi\}_r \{\Phi\}_r^T \{F\} \beta \cos(\omega t - \theta) \tag{22}$$

where Φ_r is the normalized mode shape or the eigenvector of the mode, σ_r is the decay rate and β is the magnification factor which can be expressed as:

$$\beta = 1/\sqrt{(\omega_o^2 - \omega^2)^2 + (2\sigma_r \omega)^2} \tag{23}$$

This explains that when a vortex frequency is near to the model's natural frequency the term $\omega_o^2 - \omega^2$ in Equation (23) is being eliminated, producing the largest amount of magnification. Hence, the larger term, β, will then maximize the amplitude vector, y. In this study, the vibrational amplitude of 19 m/s wind speed generating 75.8 Hz of vortex frequency is the nearest to the model's first natural frequency of 76 Hz, thus giving the largest vibrational amplitude.

Referring to Section 4.2 and Table 4, as the resultant vibrational frequency stayed between 20 and 100 Hz only the first 2 natural modes of the structure are observed to be contributing. Displayed in Figure 18 the trend of VIV amplitude to wind speed is a bell curve. Increment in vibrational amplitude occurred with the increment of wind speed until it reached the highest point during 19 m/s wind speed then proceeded to decrease. This phenomenon can well be explained by resonance theory when referred to Table 4. When vortex and vibrational frequency is near to the model's natural frequency, higher vibrational amplitude is being produced. Vortex frequency of 75.758 Hz produced at 19 m/s is almost similar to the model's natural frequency of 76.9 Hz, resonance occur, thus producing highest VIV amplitude with maximum value reaching 2.09 mm and a RMS value of 1.26 mm. Wind speed past 19 m/s showed a decrease in VIV amplitude as the vortex frequency values generated shy away from the model's natural frequency. 25 m/s wind speed having 100 Hz vortex frequency is far away from the model's natural frequency and received less contribution from the vibrational mode hence vibrating at relatively lower VIV amplitude although having a higher level of fluctuating lift force.

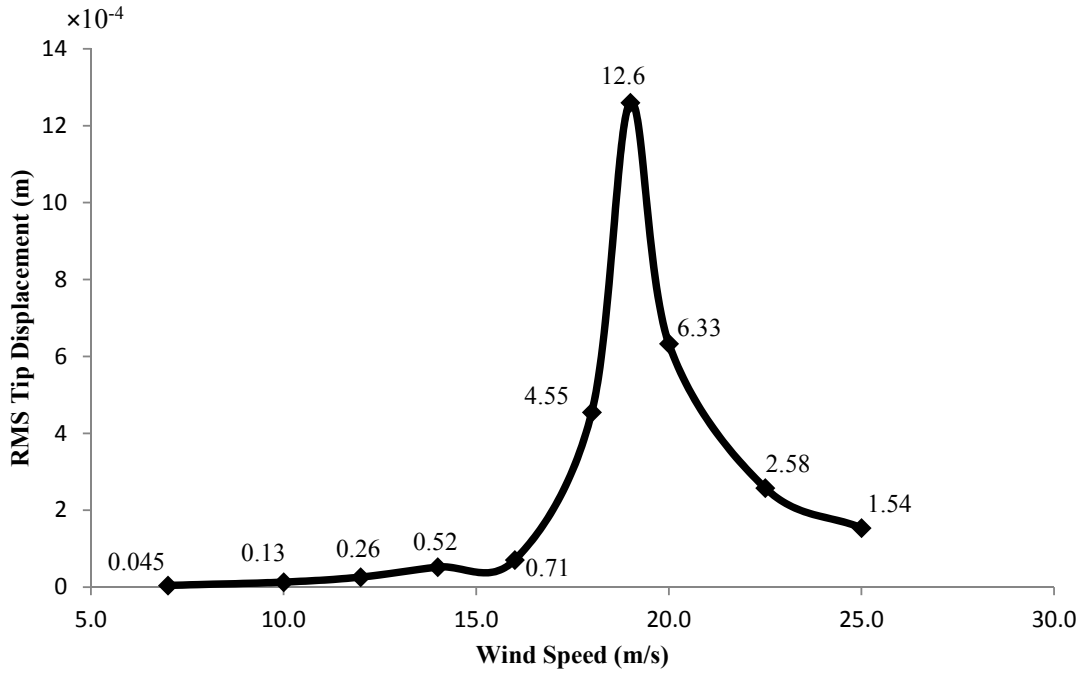

Figure 18. Graph of vibrational amplitude of the model vs. wind speed.

It is noted in this research that vortex frequency is more influential than lift force in affecting the amplitude of vortex induced vibration. Although higher wind speeds of 20, 22.5 and 25 m/s produced larger lift force acting on the flexible PVEH plate, the vibrational amplitude generated was not as high as 19 m/s wind speed because the vortex frequency produced does not resonate with the model's natural frequency. Referring to Figure 18, RMS vibrational amplitude of PVEH plate increased from 19 m/s with 1.26 mm to 20 m/s with 0.633 mm by a margin of 49.76%. Comparison could be made between 20 and 22.5 m/s where 20 m/s wind speed produced VIV with an amplitude of 0.633 mm while 22.5 m/s wind speed only achieved 0.258 mm although the latter applies 0.03 N more lift force. 20 m/s wind speed produced a vortex frequency of 80.808 Hz, which is nearer to the fundamental frequency of 76.9 Hz compared to a 22.5 m/s wind speed with a vortex frequency of 82.418 Hz. 25 m/s wind speed showed slight twisting in structural vibrational pattern compared to 19 m/s wind speed results shown in Figure 19 which is a pure bending mode. This is because the vortex frequency value of 100 Hz from 25 m/s wind speed moved away from the model's fundamental frequency but started approaching the structure's second natural frequency, creating the slight contribution of second vibrational mode or the first twisting mode onto the vibration pattern although the first bending mode is still the dominant vibrational pattern.

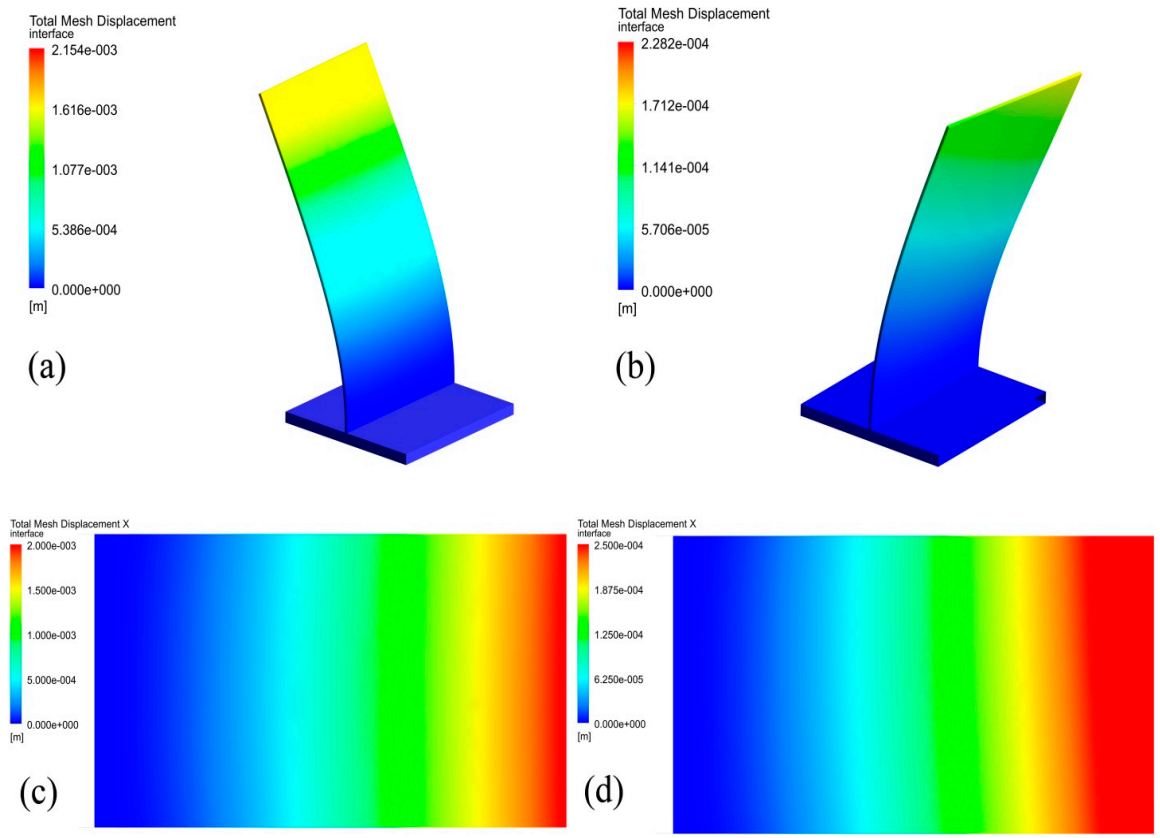

Figure 19. Deflection contour of model (**a**) 19 m/s isometric (**b**) 25 m/s isometric (**c**) 19 m/s top (**d**) 25 m/s top.

4.6. PVEH Performance

The frequency, force and displacement value for each wind speed and the load resistance applied is used to obtain the voltage and power performance when the model is under the influence of vortex induced vibration through experimental and simulation. The range of frequency used in both experiment and simulation is from 20 to 100 Hz which is within the frequency range of the first natural frequency. The second natural frequency of 480 Hz is far away and required higher wind velocity

that is hardly achievable in applications even with forced wind devices. In order to obtain the highest power output for each individual wind speed, the optimum resistance load is obtained from impedance analyzer as shown in Figure 20. For higher wind speeds, (i.e., higher vibrating frequency) the resultant optimum resistant load decreases until a local minimum at-resonant frequency, however after passing that point the resistance increases to a local maximum before going down again. The voltage generated by the PVEH plate in respective cases is then obtained through both electromechanical FSI simulation and experimental procedures. A graph of both wind speed and vibrational frequency against voltage is plotted in Figure 21a,b indicates that the pattern of both experimental and simulated result has the highest voltage generated is at 19 m/s, (i.e., 75.758 Hz). The result from experimental is 10.85 V or equivalent to 7.758 V lower than the results generated from simulation which is 18.608 V.

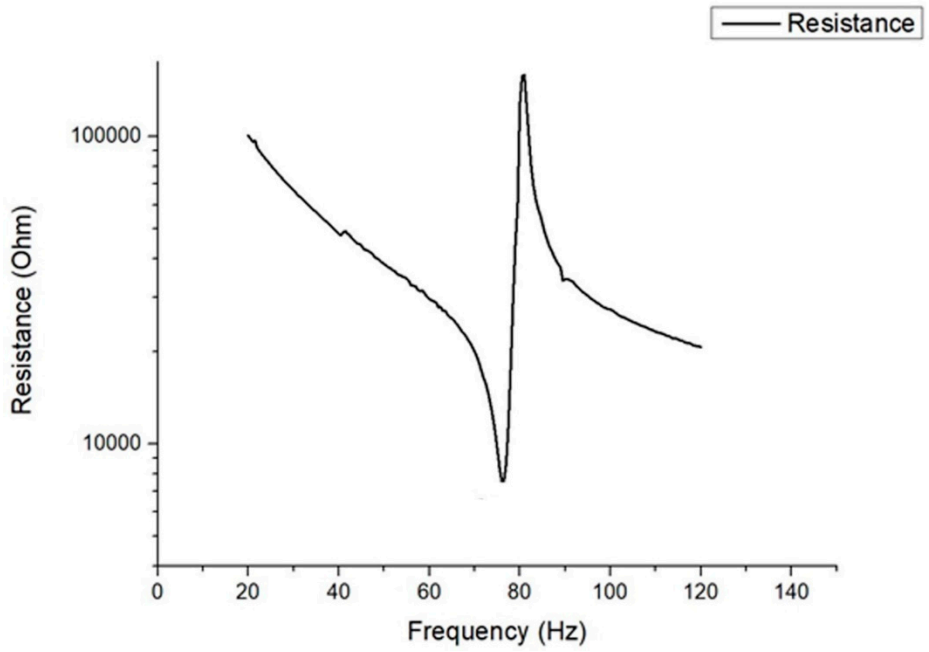

Figure 20. Graph of Optimal Resistance against Frequency obtained from Impedance Analyzer.

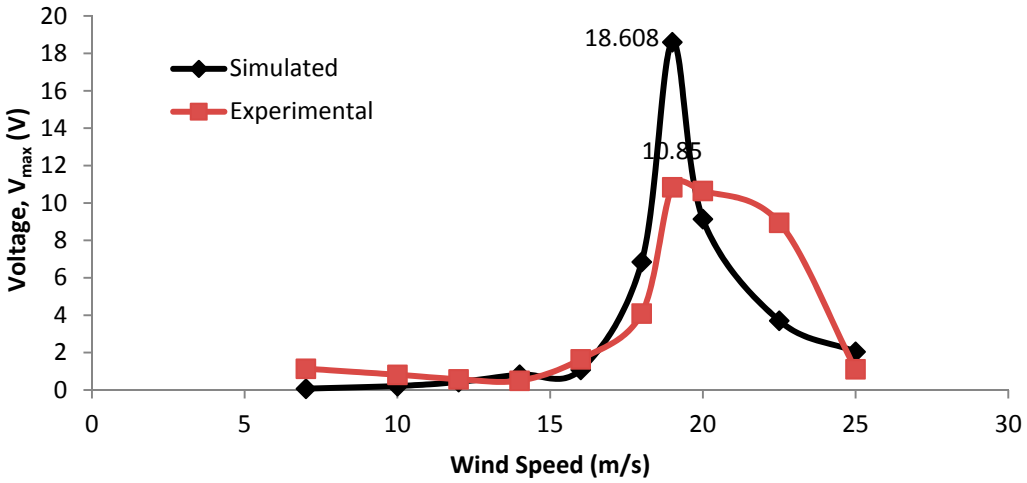

(**a**)

Figure 21. *Cont.*

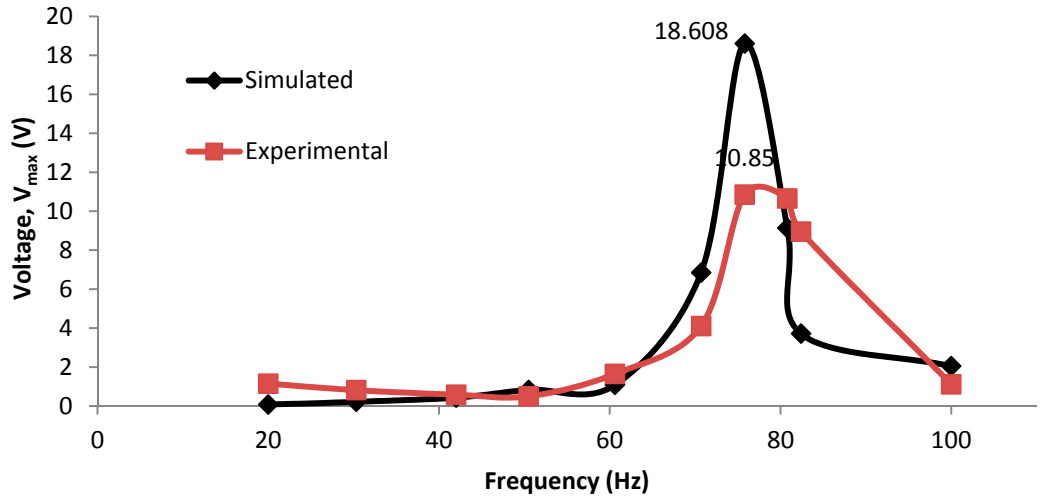

(**b**)

Figure 21. Voltage against (**a**) wind speed (**b**) frequency.

Implementing Equation (19), and combining both the optimal load resistance and voltage results obtained above, the optimum output power at each wind speed is generated. By plotting output power against wind speed or frequency as shown in Figure 22, the highest optimum power generated in simulation is recorded at 12.038 mW at wind speed of 19 m/s, (i.e., 75.758 Hz) due to matched vortex frequency and natural frequency. The experimental results show a higher output power of 15.584 mW, with an increment of 22.7%.

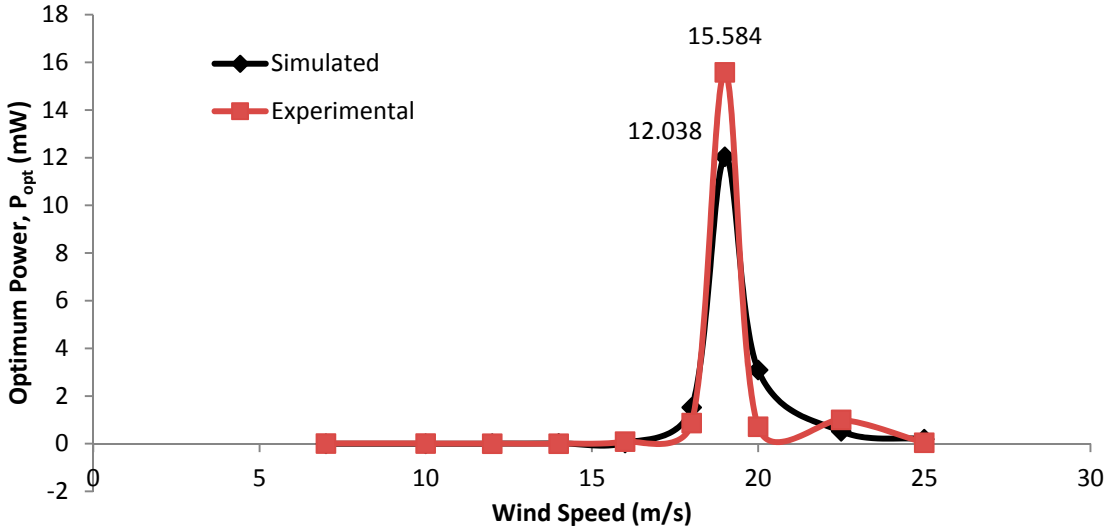

(**a**)

Figure 22. *Cont.*

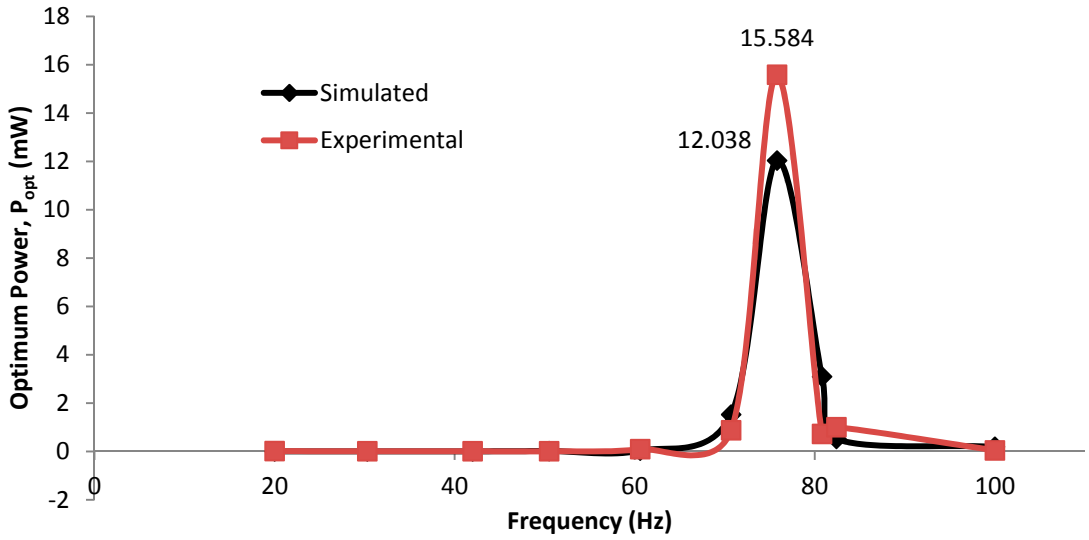

(**b**)

Figure 22. Optimum power against (**a**) wind speed (**b**) frequency.

Normalized power—also known as the average power per unit volume—and acceleration at each respective frequency is computed from the optimum power value above and is shown in Figure 23. The experimental result shows that the maximum normalized power is recorded at a value of 13.439 mW/cm^{3}g^2 under the wind speed of 19 m/s, (i.e., 75.758 Hz) while the simulated result shows the highest normalized power of 10.595 mW/cm^{3}g^2 at same wind speed of 19 m/s, which gives a difference of 21.16% between experiment and simulation.

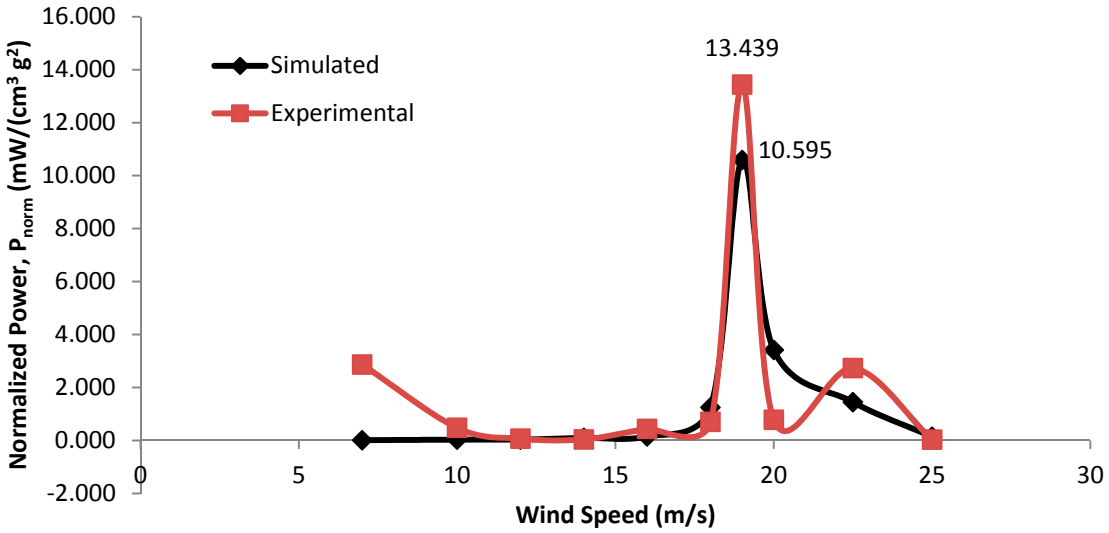

(**a**)

Figure 23. *Cont.*

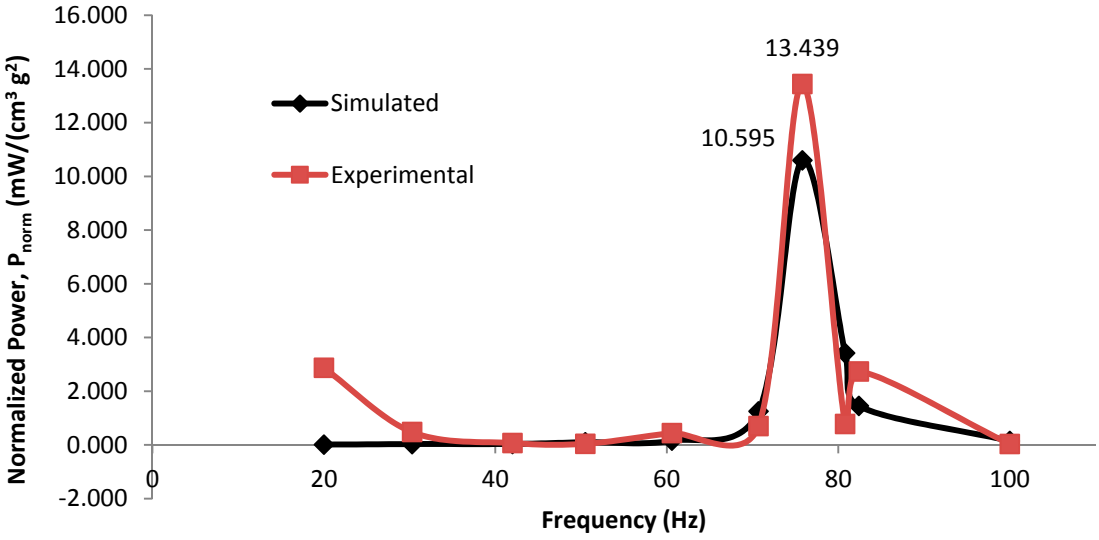

(**b**)

Figure 23. Normalized power against (**a**) wind speed (**b**) frequency.

The difference in output voltage, output power and normalized power results between experiment and simulation is probably due to the variation in modeling and the definition of the boundary conditions of the coupled bluff splitter body and PVEH plate in the simulation environment. As the model in simulation is modeled using a designated condition, while during experimental studies slight changes such as bonding of piezoelectric material and brass being ignored, the clamping of the structural model and resulting vibrational pattern have caused differences in data. The modal analysis result in Section 4.1 also discussed the difference between 2 models in which the actual PVEH plate has a higher natural frequency of 80 Hz. This has an effect on the difference in output power obtained between simulation and experimental results.

4.7. Comparison with Previous Research

For a comparison of the results, few investigations on vortex induced vibration using piezoelectric harvesting are referred to. Zhang et al., Tsujiura et al., and Koyvanich et al. did not consider bluff splitter body while Akaydin et al. used small cylindrical bluff splitter body installed at the tip acting as a tip mass in reducing the natural frequency of the model. The results are displayed in Table 5. As shown below the current study, which considers the effect of matched vortex frequency and natural frequency through the introduction of T-shape bluff splitter body, produces the highest normalized power. This is because the model is vibrating near to the natural frequency of the model causing highest vibrational displacement.

Table 5. Comparison of current study to other research results.

Author	Wind Speed (m/s)	Frequency (Hz)	Power (μW)	Normalized Power (μW/g²)
Zhang et al. [55]	1.05	26.37	0.0007	2.20×10^{-6}
Tsujiura et al. [56]	8.00	67.00	36.4	3.09×10^{-4}
Koyvanich et al. [57]	6.80	0.40	0.18	5.93×10^{-2}
Akaydin et al. [29]	1.19	3.14	100	1.74×10
Current work	19	75.758	1.56×10^{4}	1.344×10^{4}

5. Conclusions

In conclusion, the piezoelectric VIV harvester from this research implements a T-shaped design with a fixed bluff splitter body attached to a cantilever PVEH plate, in order to increase the aspect ratio for better flow separation and to further improve the quality of vortex generated. It is shown that with the presence of a bluff splitter body, the aspect ratio of the structure increases to a value of 15 henceforth the vortex generated is more visible and well defined compared to a single PVEH plate. The results show that with the same model design and a constant supply of wind flow, variance in wind speed does not affect the vortex formation length, but it will change the vortex frequency and fluctuating lift force acting on the model. It is shown from the results discussed above that, 19 m/s wind speed yields vortex frequency of 75.758 Hz, nearest to the structural modal's natural frequency with −1.48% differences. Hence the structural model undergoes resonance, producing the highest RMS VIV amplitude of 1.26 mm with a 49.76%-times increment when compared to 20 m/s case. This research deduced that a model's VIV frequency tends to lock-in to the vortex frequency and the contribution of resultant vortex frequency is larger than the fluctuating lift force in improving the vibrational amplitude. In order to achieve significantly larger vibrational amplitude, it is more important to synchronize the vortex frequency with the model's natural frequency rather than only increase the wind speed to get a larger lift force which does not guarantee a larger amplitude accomplishment. In terms of experimental electrical performance, it is also concluded that when vibrational frequency is nearer to the structure's natural frequency, the voltage output is higher than the non-synchronized ones. When coupled with the optimum impedance value, the PVEH plate produces the largest normalized power of 13.44 mW/cm^3g^2 when the vibrating frequency of 75.758 Hz resonates with the PVEH plate's fundamental natural frequency. Hence, it is proven that by installing the designed T-shaped VIV energy harvester at an optimum forced wind speed condition coupled with optimum load, a significant amount of power is able to be induced.

It is proven above that matching natural frequency to the vortex frequency enables generation of the maximum voltage, therefore in future efforts to reduce the overall structure's natural frequency could be focused on lowering the wind speed required to achieve the resonant frequency, thus improving performance when installed in conventional exhaust air cooling towers that generate lower exhaust air velocity. A prototype could also be fabricated to conduct wind tunnel and on-site tests in the future to further justify the practicality of the VIV harvesters in real life application. Finally, more factors that will affect the VIV performance such as the aspect ratios of the model, design of bluff splitter body, the model arrays and many more will be investigated and compiled in the future.

Acknowledgments: The authors wish to acknowledge the financial support and advice given by Postgraduate Research Grant (PG005-2015A), Fundamental Research Grant Scheme (FP010-2014A), Advanced Shock and Vibration Research (ASVR) Group of University of Malaya and other project collaborators. The authors also wish to thank Ya-Lun Cheng and Yuan-Long Zhuang for helping the experimental measurements.

Author Contributions: This study was initiated and designed by Zhi Chao Ong. Yu-Hsi Huang set-up experimental platform and conducted the experiments. Wei Ken Chin and Keen Kuan Kong were responsible in numerical simulations. All authors contributed in analyzing the simulation and experimental results. Zhi Chao Ong and Wei Ken Chin wrote the paper and all authors contributed in revising the paper.

Conflicts of Interest: The authors declare no conflict of interest.

References

1. Abed, I.; Kacem, N.; Bouhaddi, N.; Bouazizi, M. Nonlinear dynamics of magnetically coupled beams for multi-modal vibration energy harvesting. In Proceedings of SPIE Smart Structures and Materials + Nondestructive Evaluation and Health Monitoring, Las Vegas, NV, USA, 20–24 March 2016. [CrossRef]
2. Mahmoudi, S.; Kacem, N.; Bouhaddi, N. Enhancement of the performance of a hybrid nonlinear vibration energy harvester based on piezoelectric and electromagnetic transductions. *Smart Mater. Struct.* **2014**, *23*, 075024. [CrossRef]
3. Blevins, R.D. *Flow-Induced Vibration*; Krieger Publishing Company: Malabar, FL, USA, 2001.

4. Bearman, P.W. Vortex shedding from oscillating bluff-bodies. *Annu. Rev. Fluid Mech.* **1984**, *16*, 195–222. [CrossRef]
5. Bearman, P.W. Circular cylinder wakes and vortex-induced vibrations. *J. Fluids Struct.* **2011**, *27*, 648–658. [CrossRef]
6. Sarpkaya, T. A critical review of the intrinsic nature of vortex-induced vibrations. *J. Fluids Struct.* **2004**, *19*, 389–447. [CrossRef]
7. Williamson, C.H.K.; Govardhan, R. Vortex-induced vibrations. *Annu. Rev. Fluid Mech.* **2004**, *36*, 413–455. [CrossRef]
8. Cooper, K.R.; Wardlaw, R.L. Aeroelastic instabilities in wakes. In Proceedings of the Third International Conference on Wind Effects on Buildings and Structures, Tokyo, Japan, 1971; pp. 647–655.
9. Bernitsas, M.M.; Raghavan, K.; Ben-Simon, Y.; Garcia, E.M.H. Vivace (vortex induced vibration aquatic clean energy): A new concept in generation of clean and renewable energy from fluid flow. *J. Offshore Mech. Arct.* **2008**, *130*, 041101. [CrossRef]
10. Lee, J.H.; Bernitsas, M.M. High-damping, high-reynolds VIV tests for energy harnessing using the vivace converter. *Ocean Eng.* **2011**, *38*, 1697–1712. [CrossRef]
11. Raghavan, K.; Bernitsas, M.M. Enhancement of high damping VIV through roughness distribution for energy harnessing at $8 \times 10^3 < \mathrm{Re} < 1.5 \times 10^5$. In Proceedings of the 27th International Conference on Offshore Mechanics and Arctic Engineering, Estoril, Portugal, 15–20 June 2008; Volume 6, pp. 871–882.
12. Raghavan, K.; Bernitsas, M.M.; Maroulis, D.E. Effect of bottom boundary on VIV for energy harnessing at $8 \times 10^3 < \mathrm{Re} < 1.5 \times 10^5$. *J. Offshore Mech. Arct.* **2009**, *131*, 031102.
13. Sun, H.; Kim, E.S.; Nowakowski, G.; Mauer, E.; Bernitsas, M.M. Effect of mass-ratio, damping, and stiffness on optimal hydrokinetic energy conversion of a single, rough cylinder in flow induced motions. *Renew. Energy* **2016**, *99*, 936–959. [CrossRef]
14. Zhang, J.; Liu, F.; Lian, J.J.; Yan, X.; Ren, Q.C. Flow induced vibration and energy extraction of an equilateral triangle prism at different system damping ratios. *Energies* **2016**, *9*, 938. [CrossRef]
15. Ding, L.; Zhang, L.; Wu, C.M.; Mao, X.R.; Jiang, D.Y. Flow induced motion and energy harvesting of bluff bodies with different cross sections. *Energy Convers. Manag.* **2015**, *91*, 416–426. [CrossRef]
16. Sayeed-Bin-Asad, S.; Lundström, T.; Andersson, A. Study the flow behind a semi-circular step cylinder (laser doppler velocimetry (LDV) and computational fluid dynamics (CFD)). *Energies* **2017**, *10*, 332. [CrossRef]
17. Karbasian, H.R.; Esfahani, J.A.; Barati, E. The power extraction by flapping foil hydrokinetic turbine in swing arm mode. *Renew. Energy* **2016**, *88*, 130–142. [CrossRef]
18. Karbasian, H.R.; Esfahani, J.A.; Barati, E. Simulation of power extraction from tidal currents by flapping foil hydrokinetic turbines in tandem formation. *Renew. Energy* **2015**, *81*, 816–824. [CrossRef]
19. Shan, X.; Deng, J.; Song, R.; Xie, T. A piezoelectric energy harvester with bending-torsion vibration in low-speed water. *Appl. Sci.* **2017**, *7*, 116. [CrossRef]
20. Sohankar, A. A les study of the flow interference between tandem square cylinder pairs. *Theor. Comp. Fluid Dyn.* **2014**, *28*, 531–548. [CrossRef]
21. Pang, J.H.; Zong, Z.; Zou, L.; Wang, Z. Numerical simulation of the flow around two side-by-side circular cylinders by ivcbc vortex method. *Ocean Eng.* **2016**, *119*, 86–100. [CrossRef]
22. Kondo, N. Three-dimensional computation for flow-induced vibrations of an upstream circular cylinder in two tandem circular cylinders. *Int. J. Comput. Fluids D* **2014**, *28*, 461–476. [CrossRef]
23. Sun, H.; Ma, C.; Kim, E.S.; Nowakowski, G.; Mauer, E.; Bernitsas, M.M. Hydrokinetic energy conversion by two rough tandem-cylinders in flow induced motions: Effect of spacing and stiffness. *Renew. Energy* **2017**, *107*, 61–80. [CrossRef]
24. Derakhshandeh, J.F.; Arjomandi, M.; Cazzolato, B.S.; Dally, B. Effect of a rigid wall on the vortex induced vibration of two staggered circular cylinders. *J. Renew. Sustain. Energy* **2014**, *6*, 033114. [CrossRef]
25. Goushcha, O.; Akaydin, H.D.; Elvin, N.; Andreopoulos, Y. Energy harvesting prospects in turbulent boundary layers by using piezoelectric transduction. *J. Fluids Struct.* **2015**, *54*, 823–847. [CrossRef]
26. McCarthy, J.M.; Deivasigamani, A.; John, S.J.; Watkins, S.; Coman, F.; Petersen, P. Downstream flow structures of a fluttering piezoelectric energy harvester. *Exp. Therm. Fluid Sci.* **2013**, *51*, 279–290. [CrossRef]
27. McCarthy, J.M.; Deiyasigamani, A.; Watkins, S.; John, S.J.; Coman, F.; Petersen, P. On the visualisation of flow structures downstream of fluttering piezoelectric energy harvesters in a tandem configuration. *Exp. Therm. Fluid Sci.* **2014**, *57*, 407–419. [CrossRef]

28. McCarthy, J.M.; Watkins, S.; Deivasigamani, A.; John, S.J.; Coman, F. An investigation of fluttering piezoelectric energy harvesters in off-axis and turbulent flows. *J. Wind Eng. Ind. Aerodyn.* **2015**, *136*, 101–113. [CrossRef]
29. Akaydin, H.D.; Elvin, N.; Andreopoulos, Y. The performance of a self-excited fluidic energy harvester. *Smart Mater. Struct.* **2012**, *21*. [CrossRef]
30. Dai, H.; Abdelkefi, A.; Ni, Q.; Wang, L. Modeling and identification of circular cylinder-based piezoaeroelastic energy harvesters. *Energy Proc.* **2014**, *61*, 2818–2821. [CrossRef]
31. Huynh, B.; Tjahjowidodo, T.; Zhong, Z.; Wang, Y.; Srikanth, N. Nonlinearly enhanced vortex induced vibrations for energy harvesting. In Proceedings of the 2015 IEEE International Conference on Advanced Intelligent Mechatronics, Busan, Korea, 7–11 July 2015; pp. 91–96.
32. Alhadidi, A.H.; Abderrahmane, H.; Daqaq, M.F. Exploiting stiffness nonlinearities to improve flow energy capture from the wake of a bluff body. *Physica D* **2016**, *337*, 30–42. [CrossRef]
33. Song, R.; Shan, X.; Lv, F.; Li, J.; Xie, T. A novel piezoelectric energy harvester using the macro fiber composite cantilever with a bicylinder in water. *Appl. Sci.* **2015**, *5*, 1942–1954. [CrossRef]
34. Allen, J.J.; Smits, A.J. Energy harvesting eel. *J. Fluids Struct.* **2001**, *15*, 629–640. [CrossRef]
35. Huang, Y.H. Electromechanical coupling efficiency of transverse vibration in piezoelectric plates according to electrode configuration. *J. Chin. Inst. Eng.* **2013**, *36*, 842–855. [CrossRef]
36. Huang, Y.H.; Ma, C.C. Experimental and numerical investigations of vibration characteristics for parallel-type and series-type triple-layered piezoceramic bimorphs. *IEEE Trans. Ultrason. Ferroelectr. Freq. Control* **2009**, *56*, 2598–2611. [CrossRef] [PubMed]
37. Krushynska, A.; Meleshko, V.; Ma, C.C.; Huang, Y.H. Mode excitation efficiency for contour vibrations of piezoelectric resonators. *IEEE Trans. Ultrason. Ferroelectr. Freq. Control* **2011**, *58*, 2222–2238. [CrossRef] [PubMed]
38. Ma, C.C.; Lin, Y.C.; Huang, Y.H.; Lin, H.Y. Experimental measurement and numerical analysis on resonant characteristics of cantilever plates for piezoceramic bimorphs. *IEEE Trans. Ultrason. Ferroelectr. Freq. Control* **2007**, *54*, 227–239. [CrossRef] [PubMed]
39. Chong, W.T.; Yip, S.Y.; Fazlizan, A.; Poh, S.C.; Hew, W.P.; Tan, E.P.; Lim, T.S. Design of an exhaust air energy recovery wind turbine generator for energy conservation in commercial buildings. *Renew. Energy* **2014**, *67*, 252–256. [CrossRef]
40. Chong, W.T.; Poh, S.C.; Fazlizan, A.; Yip, S.Y.; Chang, C.K.; Hew, W.P. Early development of an energy recovery wind turbine generator for exhaust air system. *Appl. Energy* **2013**, *112*, 568–575. [CrossRef]
41. Chong, W.T.; Hew, W.P.; Yip, S.Y.; Fazlizan, A.; Poh, S.C.; Tan, C.J.; Ong, H.C. The experimental study on the wind turbine's guide-vanes and diffuser of an exhaust air energy recovery system integrated with the cooling tower. *Energy Convers. Manag.* **2014**, *87*, 145–155. [CrossRef]
42. Hensley, J.C. *Cooling Tower Fundamental*, 2nd ed.; SPX Cooling Technologies, Inc.: Overland Park, KS, USA, 2009.
43. Gulvanessian, H. En1991 eurocode 1: Actions on structures. *Proc. Inst. Civ. Eng. Civ. Eng.* **2001**, *144*, 14–22.
44. Kärnä, T. Damping methods to mitigate wind-induced vibrations. *J. Struct. Mech.* **2009**, *42*, 38–47.
45. Flaga, A.; Lipecki, T. Code approaches to vortex shedding and own model. *Eng. Struct.* **2010**, *32*, 1530–1536. [CrossRef]
46. Fail, R.; Lawford, J.A.; Eyre, R.C.W. *ARC Techncial Report. Low-Speed-Experiments: On the Wake Characteristics of Flat Plates Normal to an Air Stream*; H.M. Stationery Office: London, UK, 1959.
47. Stokes, A.N.; Welsh, M.C. Flow-resonant sound interaction in a duct containing a plate. 2. Square leading-edge. *J. Sound Vib.* **1986**, *104*, 55–73. [CrossRef]
48. Hehn, T.; Manoli, Y. *CMOS Circuits for Piezoelectric Energy Harvesters: Efficient Power Extraction, Interface Modeling and Loss Analysis*; Springer: Amsterdam, The Netherlands, 2014.
49. Akaydin, H.D.; Elvin, N.; Andreopoulos, Y. Energy harvesting from highly unsteady fluid flows using piezoelectric materials. *J. Intell. Mater. Syst. Struct.* **2010**, *21*, 1263–1278. [CrossRef]
50. Tabesh, A.; Fréchette, L.G. On the Concepts of Electrical Damping and Stiffness in Design of a Piezoelectric Bending Beam Energy Harvester. Available online: https://www.researchgate.net/publication/265865792_ON_THE_CONCEPTS_OF_ELECTRICAL_DAMPING_AND_STIFFNESS_IN_THE_DESIGN_OF_A_PIEZOELECTRIC_BENDING_BEAM_ENERGY_HARVESTER (accessed on 31 August 2017).

51. Wallin, S.; Johansson, A.V. An explicit algebraic Reynolds stress model for incompressible and compressible turbulent flows. *J. Fluids Mech.* **2000**, *403*, 89–132. [CrossRef]
52. Huang, Y.H.; Ma, C.C.; Li, Z.Z. Investigations on vibration characteristics of two-layered piezoceramic disks. *Int. J. Solids Struct.* **2014**, *51*, 227–251. [CrossRef]
53. Huera-Huarte, F.J. On splitter plate coverage for suppression of vortex-induced vibrations of flexible cylinders. *Appl. Ocean Res.* **2014**, *48*, 244–249. [CrossRef]
54. Kovasznay, L.S.G. In Hot-wire investigation of the wake behind cylinders at low reynolds numbers. *Proc. R. Soc. Lond. Ser. A Math. Phys. Sci.* **1949**, *198*, 174–190. [CrossRef]
55. Zhang, M.; Wang, J. Experimental study on piezoelectric energy harvesting from vortex-induced vibrations and wake-induced vibrations. *J. Sens.* **2016**. [CrossRef]
56. Tsujiura, Y.; Suwa, E.; Nishi, T.; Kurokawa, F.; Hida, H.; Kanno, I. Airflow energy harvester of piezoelectric thin-film bimorph using self-excited vibration. *Sens. Actuator A-Phys.* **2017**, *261*, 295–301. [CrossRef]
57. Koyvanich, K.; Smithmaitrie, P.; Muensit, N. Perspective microscale piezoelectric harvester for converting flow energy in water way. *Adv. Mater.* **2015**, *6*, 538–543. [CrossRef]